# MOCASSIN: a fully three-dimensional Monte Carlo photoionization code

B. Ercolano,★ M. J. Barlow, P. J. Storey and X.-W. Liu†

*University College London, Gower Street, London WC1E 6BT*

**ABSTRACT**

The study of photoionized environments is fundamental to many astrophysical problems. Up to the present most photoionization codes have numerically solved the equations of radiative transfer by making the extreme simplifying assumption of spherical symmetry. Unfortunately very few real astronomical nebulae satisfy this requirement. To remedy these shortcomings, a self-consistent, three-dimensional radiative transfer code has been developed using Monte Carlo techniques. The code, MOCASSIN, is designed to build realistic models of photoionized nebulae having arbitrary geometry and density distributions, with both the stellar and diffuse radiation fields treated self-consistently. In addition, the code is capable of treating one or more exciting stars located at non-central locations.

The gaseous region is approximated by a cuboidal Cartesian grid composed of numerous cells. The physical conditions within each grid cell are determined by solving the thermal equilibrium and ionization balance equations. This requires a knowledge of the local primary and secondary radiation fields, which are calculated self-consistently by locally simulating the individual processes of ionization and recombination. The structure and the computational methods used in the MOCASSIN code are described in this paper.

MOCASSIN has been benchmarked against established one-dimensional spherically symmetric codes for a number of standard cases, as defined by the Lexington/Meudon photoionization workshops: at Meudon in 1985 and at Lexington in 1995 and 2000. The results obtained for the benchmark cases are satisfactory and are presented in this paper. A performance analysis has also been carried out and is discussed here.

**Key words:** atomic processes – ISM: abundances – H II regions – planetary nebulae: general.

## 1 INTRODUCTION

Amongst the first numerical models for photoionized gaseous nebulae were those calculated by Flower (1968), Harrington (1968) and Rubin (1968). These early models included the basic physical processes of ionization and recombination of hydrogen and helium, thermal balance and escape of the emitted photons from the nebula. However, the success of these models was heavily limited by the lack of reliable atomic data, as well as by the fact that a number of important physical processes, such as charge exchange and dielectronic recombination (Aldrovandi & Péquignot 1973; Péquignot, Stasinska & Aldrovandi 1978; Storey 1981), were not accounted for at the time. The evolution of photoionization modelling has gone hand in hand with advances made in atomic physics and computer technology. The application of photoionization models to a wider range of ions has been aided by the photoionization cross-section

calculations by Reilman & Manson (1979) and, more recently, by the Opacity Project (Hummer et al. 1993). Compilations based on the latter's data (e.g. Verner & Yakovlev 1995) have made possible the inclusion of accurate photoionization cross-sections for many more ions in calculations. Mendoza (1983) presented a compilation of radiative and collisional data for collisionally excited ultraviolet, optical and infrared lines which was widely adopted, with some of these data still in use today, though most have been superseded by more recent calculations such as the *R*-matrix calculations of the Iron Project (Hummer et al. 1993) and the Belfast group (e.g. McLaughlin & Bell 1998; Ramsbottom, Bell & Keenan 1998). Currently, radiative and dielectronic recombination rates are still highly uncertain or unavailable for some ions; recent efforts to improve the situation have been reviewed by Nahar & Pradhan (1999) and Nahar (2000). Most photoionization models include temperature-dependent analytical fits to these recombination rates, such as those of Aldrovandi & Péquignot (1973) for radiative and high-temperature dielectronic recombination, and those of Nussbaumer & Storey (1983) for low-temperature dielectronic recombination.

Available computer power has increased enormously since the dawn of photoionization modelling. This has allowed more complex

★E-mail: be@star.ucl.ac.uk
†Current address: Department of Astronomy, Peking University, Beijing 100871, China.

models to be built, including more ions, more frequency points, more lines and more atomic levels. Nevertheless, the fundamental assumption of spherical symmetry has always been retained. However, a glance at an image of any Galactic H II region will immediately demonstrate that these objects are neither spherically symmetric nor homogeneous. In addition, they usually have multiple exciting stars located at non-central positions in the nebula. By contrast, planetary nebulae (PNe) have only a single, centrally located, exciting star. However, even for PNe, spherical symmetry is not a realistic assumption, as demonstrated by observations with instruments such as the *Hubble Space Telescope*, which reveal an overwhelming variety in the shapes of planetary nebulae. These objects are very rarely circular in projection; a recent study inferred that about 50 per cent of all known planetary nebulae are low-eccentricity ellipticals, while only about 10 per cent are circular in projection, with the remainder having more extreme elliptical or bipolar geometries (Soker 1997, 2001). Some objects, for example the two young planetary nebulae He 2-47 and PN M1-37 (also dubbed the *starfish twins*; Sahai 2000), show even more complicated geometries, with multiple lobes. Other PNe have fast, low-ionization emitting regions (FLIERs; Balick et al. 1993, 1994, 1998), bipolar, rotating, episodic jets (BRETs; e.g. Lopez, Meaburn & Palmer 1993), ansae, jets, knots, filaments, tails or multiple envelopes (see e.g. García-Segura 1997; Corradi et al. 1999; Perinotto 2000).

To our knowledge, only two three-dimensional photoionization codes have been developed so far, one by Baesgen, Diesch & Grewing (1990) and the other by Gruenwald, Viegas & de Broguiere (1997). The first code used a fixed number of equally sized cells and the on-the-spot approximation for the diffuse radiation field, with only the six more abundant chemical elements being taken into account. The work by Gruenwald et al. improves on this by allowing a more flexible spatial grid and by using an iterative technique for the determination of the diffuse field and also by including 12 chemical elements in the simulations.

Since most existing one-dimensional photoionization codes are based on the numerical solution of the equations of radiative transfer assuming spherical symmetry, their expansion to three dimensions can be either very difficult or impracticable, resulting in very large codes. The Monte Carlo approach to transfer problems provides a geometry-independent technique which can handle the radiation transport problem self-consistently. With this in mind, the MOCASSIN code (MOnte CArlo SimulationS of Ionized Nebulae) was developed, in order to provide a three-dimensional modelling tool capable of dealing with asymmetric and/or inhomogeneous nebulae, as well as, if required, multiple, non-centrally located exciting stars.

Section 2 contains a description of the general MOCASSIN architecture and of some of the main computational methods used in the code. The code has been benchmarked against established spherically symmetric one-dimensional photoionization codes for a set of standard nebulae, and in Section 3 we present the results of this benchmarking, together with a performance analysis of the codes. In Section 4 we discuss the results of the benchmarking and present some general guidelines on how to run the code efficiently.

## 2 DESCRIPTION OF THE MONTE CARLO CODE

### 2.1 Background

The Monte Carlo method has been widely applied to a variety of astrophysical problems, such as the penetration of ultraviolet radiation into the interiors of uniform or lumpy interstellar clouds (Flannery, Roberge & Rybicki 1980; Boissé 1990), resonance-like scattering in accretion disc winds (Knigge, Woods & Drew 1995) and polarization maps for the circumstellar envelopes of protostars (Fischer, Henning & Yorke 1994). In the examples described above the absorption and scattering coefficients are not coupled to the radiation field and, therefore, these problems do not require solution by iteration.

However, Monte Carlo techniques have also been used for dust radiative equilibrium calculations for some time – see e.g. Lefevre, Bergeat & Daniel (1982), Lefevre, Daniel & Bergeat (1983) and, more recently, Wolf, Henning & Secklum (1999). These authors use a technique in which stellar and diffuse photon packets are emitted separately; the number of diffuse photon packets (i.e. packets emitted by the dust) is determined by the dust grain temperature, which in turn is determined by the balance between the number of absorbed and emitted photon packets. An initial guess for the dust grain temperature is provided by the number of packets absorbed, and the iteration continues until the grain temperatures converge. Using this method the stellar luminosity is not automatically conserved during the Monte Carlo simulation; only after the grain temperatures have reached convergence is the stellar luminosity approximately conserved. The convergence of such codes is often very slow and requires a large number of iterations and simulation quanta in order to reach the required accuracy.

Bjorkman & Wood (2001) have described a general radiative equilibrium and temperature correction procedure for use in Monte Carlo radiative transfer codes having sources of temperature-independent opacity, such as dust. Their technique makes use of information naturally given by the Monte Carlo method, which, by tracking every photon/energy packet, makes it easy to determine where in the simulation grid energy is being absorbed. When energy is deposited at a given location, following a packet's absorption, the local medium is heated. Whenever this occurs the new local temperature is calculated and the packet is then re-emitted accordingly. The packets are followed in their path through the region, as they undergo scatterings and absorptions followed by re-emissions, with the temperatures being updated after each event, until the packets reach the edge of the nebula and escape to infinity, hence contributing to the emergent spectrum. Once all the stellar photon packets have escaped, the resulting envelope temperature and the emergent spectrum are correct without the need of any further iterations.

A great limitation of this method (Bjorkman & Wood 2001) is that it cannot be applied to situations where the opacities are temperature-dependent, as is the case in photoionized nebulae. There are two reasons for the failure of this method when the opacity varies with the local temperature: first, the number of photon packets absorbed by the cell prior to a temperature update would be either too small or too large; and, secondly, a change in temperature would also imply a change of the interaction locations of previous packets, signifying that the paths of the previous photon packets should have been different. While it is clear that, when dealing with photoionized gas, Bjorkman & Wood's technique is not applicable, their work is nevertheless very enlightening and should be taken into account for further developments of the MOCASSIN code, when a treatment for dust grains will be introduced.

A recent example of the application of the Monte Carlo technique to problems requiring solution by iteration is the work of Lucy (1999), who obtained the temperature stratification and emergent spectrum of a non-grey spherically symmetric extended stellar atmosphere in local thermodynamic equilibrium (LTE). His results show very good agreement with the predictions of Castor (1974), hence demonstrating the validity of the Monte Carlo techniques

applied, some of which were also used in the development of MOCASSIN. The current work follows the approach described by Lucy (1999) and also applied in the one-dimensional code developed by Och, Lucy & Rosa (1998). They employed a different Monte Carlo treatment of the radiative transfer in order to determine the temperature and ionization stratification iteratively for a spherically symmetric photoionized nebula of uniform density. Some of the techniques that they used are also described in detail by Lucy (1999, 2001, 2002). The basic concept is that, when calculating radiative equilibrium temperatures, conservation of stellar luminosity is more important than the details of the spectral energy distribution. With this in mind, conservation of stellar luminosity is enforced by using energy packets of constant net energy throughout the simulations. Moreover, all absorbed packets are re-emitted immediately after every absorption event. The frequencies of the re-emitted energy packets are determined by the local gas emissivities. Although the frequency distribution of the re-emitted packets will not be correct until the nebular temperatures have converged, this method naturally enforces radiative equilibrium at each point in the nebula and so naturally provides conservation of energy. This not only results in a simpler code but also makes the convergence of the gas temperatures easier (Lucy 1999, 2001). Energy packets will be discussed in more detail in Section 2.2.

## 2.2 Energy packets

The main principle of our treatment of a photoionized nebula consists of locally simulating the individual processes of ionization and recombination. The radiation field is therefore expressed in terms of energy packets, $\varepsilon(\nu)$, which are the calculation quanta. $\varepsilon(\nu)$ is a packet consisting of $n$ photons of frequency $\nu$ such that

$$\varepsilon(\nu) = nh\nu. \tag{1}$$

In addition, we take all packets to have constant energy $\varepsilon_0$. There are several reasons for choosing to work with monochromatic, indivisible packets of radiant energy instead of photons. First of all, energy packets are more computationally economic. Also, since they all have the same energy, those packets emitted in the infrared will contain a larger number of photons, which, as a consequence, will not have to be followed individually (Abbott & Lucy 1985). Note that all energy packets are followed until they escape the nebula, including infrared energy packets. This is in order to allow the introduction of dust particles into the radiative transfer treatment of MOCASSIN, which is planned for the near future. Also, as the total stellar luminosity, $L_*$, is evenly split amongst the stellar energy packets, the energy carried by a single packet in the time interval $\Delta t$, which represents the duration of the Monte Carlo experiment, is given by

$$\frac{L_*}{N} = \frac{\varepsilon_0}{\Delta t}, \tag{2}$$

where $N$ is the number of energy packets used in the simulation (Och et al. 1998). Most importantly, the use of constant energy packets is a natural way of imposing strict energy conservation at any point in the nebula (Lucy 1999). So, when a packet of radiant energy $\varepsilon(\nu_a) = \varepsilon_0$ is absorbed, it is immediately re-emitted with a frequency $\nu_e$, which is determined according to a frequency distribution set by the gas emissivity of the current cell. The packet emitted, $\varepsilon(\nu_e)$, will then have the same energy as the absorbed packet, $\varepsilon(\nu_a)$, meaning that only the number, $n$, of photons contained in the packet is changed.

## 2.3 Initiation

In our modelling the gaseous region is approximated by a three-dimensional Cartesian grid, where the ionizing source can be placed at the centre or anywhere else in the grid. This feature is very useful when dealing with axisymmetric nebulae, since, by placing the source in a corner of the grid, we need only consider one eighth of the nebula, which can then be reconstructed in full at the end of the simulation. This allows the running of models with much higher spatial resolution than those which would be possible if a full nebula had to be considered, by putting the source in the centre and, therefore, not making use of any symmetry properties of the object. Switches built inside the code allow the user to specify whether the nebula has some degree of symmetry and, if so, whether the symmetry is to be used.

Inside each grid cell, all nebular properties, such as the mass density of the gas ($\rho$), the electron temperature and density ($T_e$ and $N_e$), and the frequency-dependent gas opacity and emissivity ($\kappa_\nu$ and $j_\nu$), are constant by definition. Thermal balance and ionization equilibrium are imposed in each grid cell in order to obtain the physical conditions in the local gas.

The energy packets are created at the position of the ionizing source and they all carry the same energy $\varepsilon_0$, as discussed in the previous section. The frequency, $\nu$, of each individual packet emitted is derived from the input spectrum of the ionizing source according to the probability density function

$$p(\nu) = \frac{F_\nu \, d\nu}{\int_{\nu_{\min}}^{\nu_{\max}} F_{\nu'} \, d\nu'} = \frac{F_\nu \, d\nu}{L_* / (4\pi R_*^2)}, \tag{3}$$

where $F_\nu$ is the stellar flux and $R_*$ is the stellar radius. This is then the probability of an energy packet being emitted with a frequency lying in the interval $(\nu, \nu + d\nu)$. The upper and lower integration limits, $\nu_{\min}$ and $\nu_{max}$, have to be chosen properly, depending on the input spectrum, in order to ensure that the bulk of the radiation is included in the frequency range. As the source emits energy isotropically, the direction of travel of every energy packet emitted is chosen randomly. This is done by choosing two random numbers, $\alpha$ and $\beta$, in the interval [0, 1], and calculating the following quantities:

$$
\begin{aligned}
w &= 2\alpha - 1, \\
t &= \sqrt{1 - w^2}, \\
\theta &= \pi(2\beta - 1), \\
u &= t \cos\theta, \\
v &= t \sin\theta.
\end{aligned}
\tag{4}
$$

The random unit vector in Cartesian coordinates is then $(u, v, w)$ (Harries & Howarth 1997).

## 2.4 Trajectories

Once a stellar packet is created at the source and launched into the nebula, its trajectory must be computed as it undergoes absorptions followed by re-emissions due to bound–free and free–free processes. The trajectory ends when the packet reaches the edge of the nebula, where it escapes to infinity and contributes to the emergent spectrum.

There are two methods to track the packets and determine the locations of the absorption events. Consider a packet of frequency $\nu_p$, emitted in the direction $\hat{u}$. The first of these methods consists of calculating the run of optical depth, $\tau_{\nu_p}$, at the energy packet frequency $\nu_p$, from the location at which the packet is emitted to

the edge of the ionized region along the direction of travel, $\hat{u}$. The probability of absorption along that path is then given by

$$p(\tau_{v_p}) = e^{-\tau_{v_p}} \qquad (5)$$

and the normalized cumulative probability function is given by

$$P(l) = \frac{\int_0^{\tau_{v_p}(l)} e^{-\tau_{v_p}} \, d\tau_{v_p}}{\int_0^{\infty} e^{-\tau_{v_p}} \, d\tau_{v_p}} = 1 - e^{-\tau_{v_p}(l)}, \qquad (6)$$

where $\tau_{v_p}(l)$ is the optical depth to the absorption event and $l$ is the path-length. The position at which the energy packet will be absorbed will then be determined by choosing a random number in the interval [0, 1] and comparing it against $P(l)$. In reality, it is more convenient to use the inverse approach, where the optical depth from the energy packet source to the event can be derived from the inverse of equation (7)

$$\tau_{v_p}(l) = -\ln(1 - U_R) \qquad (7)$$

where $U_R$ is a random number in the interval [0, 1]. Once $\tau_{v_p}(l)$ has been calculated, then the path-length can be directly derived (Harries & Howarth 1997).

The second method was suggested by Lucy (1999) and it consists of testing whether an absorption event occurs, on a cell-by-cell basis. In other words, assume that, within each uniform cell, the random path of a packet between events is given by equation (7), which corresponds to a physical displacement, $l$, given by

$$\tau_{v_p} = \kappa_v \rho l, \qquad (8)$$

where $\kappa_v$ and $\rho$ are the frequency-dependent absorption coefficients and the density of the current cell respectively. The method then consists of checking whether the displacement $l$ is large enough to carry the packet out of its current cell. If this is the case, the packet is moved along its direction of travel, $\hat{u}$, up to the boundary with the adjacent cell, where a new value for $U_R$ is cast, giving a new $\tau_{v_p}$, and any further movement of the packet in this new cell is to be followed. Alternatively, if the displacement $l$ is not large enough to carry the energy packet across the next boundary, the packet will be absorbed and then re-emitted at the end-point of the displacement. Lucy also clarifies in his paper that the selection of a new value of $\tau_{v_p}$ at the crossing of a boundary does not introduce a bias since a photon always has an expected path-length to its next event corresponding to $\tau_v = 1$, regardless of the distance it might already have travelled.

In this work both methods were implemented in the code, in turn, in order to test their respective performances. The first method proved to be much more computationally expensive than the second. This is due to the fact that, in order to track down the position at which an energy packet is absorbed, using our knowledge of $\tau_{v_p}(l)$, an array searching routine has to be used to locate the index of $\tau_{v_p}(l)$ within the array of optical depths calculated from the packet's source to the edge of the nebula. Although the searching procedure employs a bisection technique, which makes it quite efficient, the large number of calls to it, as a result of the large number of energy packet interactions within a simulation, means that nearly 60 per cent of the run time is spent carrying out these searches. The second method does not require any calls to the array searching routine, as the packets are followed step by step through the nebula, and this results in the run time being considerably reduced. The current version of MOCASSIN therefore uses Lucy's approach to track the energy packets throughout the nebula.

Finally, the direction of travel of the newly emitted diffuse energy packets (i.e. those packets re-emitted immediately after an absorption event) needs to be determined. Since absorption and re-emission

are two independent events, the diffuse packets are emitted isotropically and therefore their direction of travel is chosen randomly using equation (4).

## 2.5 The mean intensity

The success of a Monte Carlo model often relies on the careful choice of appropriate *estimators*. Monte Carlo estimators provide the means to relate the quantities we *observe* during our Monte Carlo experiment to the physical quantities we want to determine. In a photoionization model, a measure of the radiation field is needed, namely the mean intensity, $J_v$.

In the work of Och et al. (1998), the Monte Carlo estimator of $J_v$ is constructed by using the definition of the specific intensity, $I_v$, in spherical coordinates, $(r, \theta)$, as a starting point:

$$\Delta E = I_v(r, \theta) \Delta A |\cos \theta| \Delta v \Delta \omega \Delta t, \qquad (9)$$

where $\Delta A$ is the reference surface element, $\theta$ is the angle between the direction of light propagation and the normal to the surface $\Delta A$, and $\Delta \omega$ is the solid angle. The mean intensity can then be obtained from this by calculating the zero-order moment of $I_v$, which gives

$$4\pi J_v(r) = \int_\Omega I_v \, d\omega = \frac{\Delta E}{\Delta t} \sum_{i=1}^{N_k} \frac{1}{\cos \theta_i} \frac{1}{\Delta A} \frac{1}{\Delta v}, \qquad (10)$$

by comparison with equation (9). The sum is over all packets $N_k$ with frequency lying in the interval $(v, v + dv)$, crossing $\Delta A$ at an angle $\theta$. As discussed above, $\Delta E / \Delta t$ represents the energy carried by a single packet in the time interval $\Delta t$, since $\Delta E = \varepsilon_0$, which is given by equation (2). Equation (10) then provides a relation between the Monte Carlo *observables*, i.e. the number of energy packets with frequency lying in the interval $(v, v + dv)$, crossing $\Delta A$ at angle $\theta$, and the mean intensity of the radiation field, which is the required physical quantity.

The use of the Och et al. (1998) estimators for $J_v$, however, becomes problematic in the non-spherically symmetric case, since the reference surface for the volume elements in an arbitrary two- or three-dimensional coordinate system might not be unique or as obvious as in the one-dimensional case. In our work, a more general expression for the estimator of $J_v$ is sought. Therefore, following Lucy's argument (Lucy 1999), an estimator for $J_v$ is constructed starting from the result that the energy density of the radiation field in the frequency interval $(v, v + dv)$ is $4\pi J_v dv/c$. At any given time, a packet contributes energy $\varepsilon(v) = \varepsilon_0$ to the volume element that contains it. Let $l$ be a packet's path-length between successive *events*, where the crossing of cell boundaries is also considered an event; the contribution to the time-averaged energy content of a volume element, due to the $l$ fragments of trajectory, is $\varepsilon_0 \, \delta t / \Delta t$, where $\delta t = l/c$. From this argument it follows that the estimator for the volume element's energy density can be written as

$$\frac{4\pi J_v \, dv}{c} = \frac{\varepsilon_0}{\Delta t} \frac{1}{V} \sum_{dv} \frac{l}{c}, \qquad (11)$$

where $V$ is the volume of the current grid cell and the summation is over all the fragments of trajectory, $l$, in $V$, for packets with frequencies lying in the interval $(v, v + dv)$. Again, a relation between Monte Carlo observables (i.e. the flight segments, $l$) and the mean intensity of the radiation field, $J_v$, has been obtained. Moreover, equation (11) is completely independent of the coordinate system used and, indeed, of the shapes of the volume elements, $V$. Another important aspect of this approach is that all packets passing through a given grid cell contribute to the local radiation field even

without being absorbed; this means that equation (11) returns estimators of the radiation field even in the extremely optically thin case when all packets pass through the nebula without any absorption events. From this argument it follows that this technique allows a much better sampling and, hence, in general, much less noisy results compared to other techniques based on estimators for which only packets *absorbed* within a given volume element count.

### 2.6 Gas emissivity and the diffusion of energy packets

As we have already discussed in previous sections, after an energy packet is absorbed, a new packet is re-emitted from the same location in a random direction. The frequency of the re-emitted packet is calculated by sampling the spectral distribution of the total local emissivity, $j_\nu^{\text{tot}}$. In order to satisfy the thermal balance implied by the Monte Carlo model, all major emission processes have to be taken into account, including the complete non-ionizing nebular continuum and line emission, since they are part of the energy budget. The non-ionizing radiation generated in the nebula is assumed to escape without further interaction and constitutes the *observable spectrum*, which can then be compared with observations. The following paragraphs are concerned with the description of the individual contributions to the total emissivity.

The continuum emission due to H I, He I, He II and heavier ions is included. The H I continuum can be divided into the Lyman continuum, which is capable of ionizing H, and the Balmer, Paschen, etc., continua, which are not capable of ionizing H. The emissivity in the Lyman continuum is calculated directly from a combination of the Saha and Milne relations:

$$j_\nu = \frac{h\nu^3}{c^2} \frac{\omega_i}{\omega_{i+1}} \left(\frac{h^2}{2\pi mkT_e}\right)^{3/2} a_\nu(X^i) e^{-h(\nu-\nu_0)/kT_e} X^{i+1} N_e, \quad (12)$$

where $\omega_i$ and $\omega_{i+1}$ are the ground-state statistical weights of the ions involved, $X^{i+1}$ is the abundance of the recombining ion $X^{i+1}$, $a_\nu(X^i)$ is the photoionization cross-section and $\nu_0$ is the photoionization threshold. The emissivity of the other series continua are obtained by interpolation of published data (Ferland 1980). A similar approach is used for the He I and the He II continua, where for frequencies greater than 1.8 and 4.0 Ryd (where 1 Ryd = $2.180 \times 10^{-18}$ J), respectively, equation (12) is used, and the emissivities at lower frequencies are obtained by interpolation of the data published by Brown & Matthews (1970) for the He I series and by Ferland (1980) for the He II series. The continuum emissivity of heavy elements is also calculated using equation (12). In the hydrogenic case (i.e. H I and He II), the two-photon continuum is calculated using the formalism described by Nussbaumer & Schmutz (1984); the data of Drake, Victor & Dalgarno (1969) are used for He I. Recombination lines between lower levels $n = 2$–8 and upper levels $n = 3$–15 for H I, and lower levels $n = 2$–16 and upper levels $n = 3$–30 for He II, are calculated as a function of temperature according to the case B data published by Storey & Hummer (1995). The He I recombination lines are calculated as a function of temperature using the data of Benjamin, Skillman & Smits (1999). In general, He I singlet lines follow case B whereas triplet lines follow case A (as there is no $n = 1$ level for the triplets). Transitions to the $1^1S$ ground state of He I produce lines that are capable of ionizing H and low-ionization stages of higher elements. In particular, the emissivities of the He I Lyman lines from $n = 2$ to $n = 5$ (Brocklehurst 1972) and the intercombination lines corresponding to the transitions $2^3S$–$1^1S$ and $2^3P$–$1^1S$ are estimated as a function of temperature using the data of Robbins (1968). The contributions due to these lines to the total energy distribution, from which the probability density functions

are derived, are added into the respective energy bins. Similarly, He II Lyman lines can ionize both neutral hydrogen and neutral helium, as well as some of the low ions of heavier elements. Therefore the emissivities of He II Lyman lines with upper levels from $n = 2$ to $n = 5$ (fits to Storey & Hummer 1995) are also estimated as a function of temperature and their contributions to the total energy distribution added into the respective frequency bin, as for the He I lines. This method is based on the fact that all emission profiles are currently treated as $\delta$ functions and the line opacity is assumed to be zero; and the absorption of energy packets is only due to the continuum opacity. Finally, the emissivities of the collisional lines of the heavier ions are calculated. This is done by using matrix inversion procedures in order to calculate the level populations of the ions. Appendix 1 contains references for the atomic data used for each ion.

The energy distribution is derived from the total emissivity, summing over all the contributions in a particular frequency interval. The non-ionizing line emission is treated separately, since, whenever such line packets are created, they escape without further interaction.[1]

Once the line and continuum emissivities have been calculated, the probability that the absorption of an ionizing energy packet will be followed by the emission of a non-ionizing packet is given by

$$P_{\text{esc}} = \frac{\sum_i j_{X^i}^l + \int_0^{\nu_H} j_\nu^c \, d\nu}{\sum_i j_{X^i}^l + \sum j_{\text{HeI}}^l + \sum j_{\text{HeII}}^l + \int_0^{\nu_{\text{max}}} j_\nu^c \, d\nu}, \quad (13)$$

where $\nu_{\text{max}}$ is the higher limit of the frequency grid, the $j_{X^i}^l$ are the emissivities of the non-ionizing recombination lines of all species considered, $j_\nu^c$ is the frequency-dependent continuum emissivity, and $j_{\text{HeI}}^l$ and $j_{\text{HeII}}^l$ are the contributions due to those recombination lines of He I and He II which are capable of ionizing neutral hydrogen and neutral helium. The choice between the re-emission of an ionizing photon or a non-ionizing one is made at this point in the code.

If an ionizing energy packet is to be re-emitted, then the new frequency will be calculated according to the normalized cumulative probability density function for the ionizing radiation, given by

$$p(\nu) = \frac{\int_{\nu_H}^\nu j_{\nu'}^c \, d\nu' + \sum j_{\text{HeI}}^l + \sum j_{\text{HeII}}^l}{\int_{\nu_H}^{\nu_{\text{max}}} j_{\nu'}^c \, d\nu' + \sum j_{\text{HeI}}^l + \sum j_{\text{HeII}}^l}, \quad (14)$$

where, as usual, the contributions due to the He I and He II lines are added in the corresponding frequency bins. If a non-ionizing energy packet is to be re-emitted, then its frequency must be determined from the probability density function for non-ionizing radiative energy, which is analogous to equation (14).

### 2.7 The iterative procedure

An initial guess of the physical conditions in the nebular cells, such as the ionization structure, electron temperature and electron density, needs to be specified before the simulation can begin. Procedures in MOCASSIN have been constructed such that only an initial guess at the electron temperature (which is initially set to a constant value throughout the nebula) must be included in the input file. MOCASSIN can then guess an initial ionization structure and, hence, the electron density. However, if the output of a one-dimensional model

---

[1] Resonance lines longward of 912 Å (e.g. C IV λλ1548,1550) may, in fact, diffuse out of the nebula via resonant scattering and may also be absorbed by dust during such diffusion. A treatment of dust grains will be included in future developments of the MOCASSIN code, and such effects may then be accounted for.

(or a combination of more than one of them) is available, there are also procedures built into MOCASSIN to map these on to the three-dimensional Cartesian grid, by using simple interpolation routines. A one-dimensional mode option was implemented in MOCASSIN for this purpose. Several tests have shown that, while the choice of the initial conditions has, of course, no influence on the final result of the simulation, it can, however, have an impact on the number of iterations required to reach convergence. It is hard to quantify the number of iterations required for convergence by each method. In particular, it depends strongly on the initial temperature input used in the first method, and, when applying the second method, on the deviation of the actual three-dimensional geometry from the simplified one-dimensional model used. However, with sufficient energy packets, the benchmark models described here should be fully converged in approximately 15–20 iterations. A strategy to speed up the simulations is described in Section 3.1.

Once the initial conditions are specified, the frequency-dependent total emissivities are calculated in each grid cell in order to set up the probability density functions for re-emitted radiation, which are used for the determination of the frequency distribution of the re-emitted energy packets during the Monte Carlo simulation. The energy packets are then fired through the grid and their trajectories computed. Once all the energy packet trajectories have been computed, the Monte Carlo estimators for the mean intensity of the stellar and the diffuse radiation fields can be obtained, as described in Section 2.5. The ionization fraction and the electron temperatures and densities must now be updated to be self-consistent with the current estimates of the radiation field at each grid point. This means solving the local ionization balance and thermal equilibrium equations simultaneously. The entire procedure is repeated until convergence is achieved. The convergence criterion that is used in this work is based on the change of the local hydrogen ionization structure between successive iterations. In some cases, however, this is not a suitable convergence criterion (e.g. in hydrogen-deficient environments). For this reason, other criteria are also implemented in the code (e.g. based on the change of the local helium ionization structure, or of the local electron temperature between successive iterations), and these can be easily selected by using the appropriate switches in the input file.

### 2.8 Comparison of the model with observations

When the model has converged to its final solution, the output spectrum can be computed and compared with the results obtained from other models or with observational data. The total luminosity of the nebula emitted in various emission lines longward of the Lyman limit can be obtained by using two methods. The first method, which is only available to Monte Carlo codes, consists of summing up the number of energy packets in the given line, $N_{\text{line}}$, over the grid cells. Hence, the power emitted in the line is given by

$$L_{\text{line}} = \frac{\varepsilon_0}{\Delta t} \sum_{i=1}^{i_{\text{max}}} \sum_{j=1}^{j_{\text{max}}} \sum_{k=1}^{k_{\text{max}}} N_{\text{line}}(x_i, y_j, z_k), \tag{15}$$

where $\varepsilon_0/\Delta t$ is given by equation (2). The second method consists of using the values of the local electron temperature and ionic abundances given by the final converged model solution to obtain the line emissivities for each grid cell. The luminosity of the nebula in any given line can then be calculated easily by summing the emissivity of the required line over the volume of the nebula.

A comparison of the results obtained using the two methods described above provides an indication of the level of accuracy achieved during the simulation, as the two methods will give con-

sistent results only if enough energy packets have been used to yield good statistics for every line. In general, the second method (formal solution) yields the most accurate results, particularly for weak lines, which may emit relatively few photons. For the benchmark cases presented here, reasonable accuracy was deemed to have been achieved when the fluxes of the strongest transitions obtained using the pure Monte Carlo method were within 10 per cent of those obtained using the formal solution. Both methods can also be used to calculate line-of-sight results and to simulate long-slit observations. However, just as for the calculation of the integrated spectrum, the formal solution method is to be preferred, as it yields the most accurate results, particularly for the weaker lines.

In addition to the integrated emergent spectrum, other useful comparisons with the observations can be carried out, e.g. projected images of the final model nebula in a given line or at a given continuum frequency can be produced for arbitrary viewing angles. These can be compared directly with nebular images obtained in an appropriate filter. MOCASSIN computes and stores the physical properties of the nebula, as well as the emissivities of the gas at each grid point; these can be fed into Interactive Data Language (IDL) plotting routines in order to produce maps (Morisset, Gruenwald & Viegas 2000). Also, by assuming a velocity field, line spectral profiles can be produced, together with position–velocity diagrams. These can be compared with observations, if available, to deduce spatio-kinematic information about the object being studied. More information about the original IDL routines is given by Morisset et al. (2000) and Monteiro et al. (2000). Details of the actual application to MOCASSIN's grid files are available in a companion paper on the modelling of the planetary nebula NGC 3918 (Ercolano et al. 2003, hereafter Paper II).

At the end of each Monte Carlo iteration the physical quantities that characterize the grid are written out to disk into three files, namely grid1.out, grid2.out and grid3.out. The first file contains the local electron temperature and density as well as the gas density at each grid cell, the second the ionization structure of the nebula, and the third a number of model parameters, including the number of energy packets to be used in the simulation. These files are used in conjunction with a *warm start* driver, which allows an interrupted simulation to be resumed from the end of the last Monte Carlo simulation. This means that, once a simulation has been interrupted, the number of energy packets used (and indeed other model parameters, if required) can be adjusted, before the simulation is restarted, by modifying the file grid3.out. This feature can be used to speed up the simulations by using the following approach. The first few iterations are run using a lower number of energy packets than actually needed; so, for example, if the optimum number of energy packets for a given model is $10^6$, then the first few iterations can be carried out using only $10^5$ packets, hence reducing the run time for these by a factor of 10. This will result in about 50–60 per cent of the grid cells converging; in general, the inner cells converge more quickly, due to the larger number of sampling units available there (mainly as a result of geometrical dilution and reprocessing of energy packets to non-ionizing energy packets). At this point the simulation is interrupted and then resumed, after having adjusted the number of energy packets to the final required value (i.e. $10^6$ in the previous example). Final convergence will then be achieved, in most cases, within four or five further iterations. The actual number of iterations required depends on the number of energy packets used: the larger the number of sampling quanta available at each cell, the quicker the cells will converge to a solution. The numbers quoted above, however, also depend on each particular model's geometry and optical thickness.

## 2.9 General architecture

The MOCASSIN code was written using the FORTRAN 90 programming language. The code was developed and run initially on a Compaq (Dec) XP1000 with a 500-MHz CPU and 1 GB of memory, and a preliminary serial version of the code still exists. A fully parallel version of the code has since been developed using Multiple Processes Interface (MPI) routines, and it currently runs on a Silicon Graphics Origin 2000 machine with 24 processors and 6 GB of memory, and on a SUN Microsystems Sunfire V880 machine with 16 processors and 64 GB of memory. Monte Carlo simulations are, by their nature, very parallelizable problems and, indeed, MOCASSIN can achieve a linear *speed-up*, i.e. a speed-up that is directly proportional to the number of processors used. A detailed description of all the MOCASSIN modules, input commands and output files is given by (Ercolano 2002). A copy of the code is available from the author (be@star.ucl.ac.uk) together with the relevant thesis chapters.

## 3 APPLICATION TO BENCHMARK CASES

Numerical simulations of photoionized nebulae are very complex and a number of factors, such as numerical approximations and assumptions, and the complexity of the calculation itself, introduce a degree of uncertainty into the results. For this reason, it is important for modellers to have certain standards of comparison, in order to identify problems in their codes and to reach an adequate degree of accuracy in their calculation. A series of meetings have been held, beginning in Meudon, France, in 1985 (Péquignot 1986) and taking in Lexington, Kentucky, USA, first in 1995 (Ferland et al. 1995) and again in 2000 (Péquignot et al. 2001), in order to define a set of benchmark cases against which all photoionization modellers could test their codes. The benchmarks that resulted from these meetings include H II regions, planetary nebulae, narrow-line regions (NLRs) of active galactic nuclei (AGNs) and X-ray slabs. MOCASSIN does not have, at present, the capability to treat NLRs and X-ray slabs, as some relevant physical processes, such as Compton heating and inner-shell ionization, are not yet included. For this reason, only the H II region and planetary nebula benchmarks are performed in this work. The expansion of the code to include high-energy processes is planned in the future.

Results from several other codes are available for comparison. These are all one-dimensional codes and, apart from differences in the atomic data used by each of them, their main differences lie in the treatment of the diffuse radiation field transfer. A brief description of each of these codes is given by Ferland et al. (1995). Although the majority of these codes have evolved somewhat since the 1995 Lexington meeting, mostly via the updating of the atomic data sets and the inclusion of more and specialized physical processes, their basic structures have stayed the same. The seven codes included for comparison are: G. Ferland's CLOUDY (GF), J. P. Harrington's code (PH), D. Péquignot's NEBU (DP), T. Kallman's XSTAR (TK), H. Netzer's ION (HN), R. Sutherland's MAPPINGS (RS) and R. Rubin's NEBULA (RR). Only two of these codes, the Harrington code and Rubin's NEBULA, treat the diffuse radiative transfer exactly. The others use some versions of the *outward-only approximation* of varying sophistication. In this approximation, all diffuse radiation is assumed to be emitted isotropically into the outward half of space.

The predicted line fluxes from each code for each benchmark case are listed in Tables 4–7, together with the volume-averaged mean electron temperature weighted by the proton and electron densities $N_p N_e$, $\langle T[N_p N_e]\rangle$, the electron temperature at the inner edge of

**Table 1.** Lexington 2000 benchmark model input parameters.[a]

| Parameter | HII40 | HII20 | PN150 | PN75 |
|---|---|---|---|---|
| $L(BB)/10^{37}$ erg s$^{-1}$ | 308.2 | 600.5 | 3.607 | 1.913 |
| $T(BB)/10^3$ K | 40 | 20 | 150 | 75 |
| $R_{in}/10^{17}$ cm | 30 | 30 | 1 | 1.5 |
| $n_H/\mathrm{cm}^{-3}$ | 100 | 100 | 3000 | 500 |
| He/H | 0.10 | 0.10 | 0.10 | 0.10 |
| C/H × 10$^5$ | 22 | 22 | 30 | 20 |
| N/H × 10$^5$ | 4 | 4 | 10 | 6 |
| O/H × 10$^5$ | 33 | 33 | 60 | 30 |
| Ne/H × 10$^5$ | 5 | 5 | 15 | 6 |
| Mg/H × 10$^5$ | – | – | 3 | 1 |
| Si/H × 10$^5$ | – | – | 3 | 1 |
| S/H × 10$^5$ | 0.9 | 0.9 | 1.5 | 1 |

[a]Elemental abundances are by number with respect to H.

the nebula, $T_{inner}$, and the mean ratio of fractional He$^+$ to fractional H$^+$, $\langle$He$^+\rangle/\langle$H$^+\rangle$, which represents the fraction of helium in the H$^+$ region that is singly ionized. $\langle T[N_p N_e]\rangle$ and $\langle$He$^+\rangle/\langle$H$^+\rangle$ are calculated according to the following equations (Ferland et al. 1995)

$$\langle T[N_p N_e]\rangle = \frac{\int N_e N_p T_e \, \mathrm{dV}}{\int N_e N_p \, \mathrm{dV}} \tag{16}$$

and

$$\frac{\langle\mathrm{He}^+\rangle}{\langle\mathrm{H}^+\rangle} = \frac{n(\mathrm{H})}{n(\mathrm{He})} \frac{\int N_e N_{\mathrm{He}^+} \, \mathrm{dV}}{\int N_e N_p \, \mathrm{dV}}, \tag{17}$$

where $N_e$ and $N_p$ are the local electron and proton densities, respectively, $N_{\mathrm{He}^+}$ is the density of He$^+$, and $n(\mathrm{H})$ and $n(\mathrm{He})$ are the total hydrogen and helium densities.

Table 1 lists the input parameters for all the benchmark models discussed here. All the benchmark cases listed in Table 1 were calculated using both the three-dimensional and the one-dimensional mode of MOCASSIN, and both sets of results are included here for comparison. It is clear from Tables 4–7 that the results of the three-dimensional and one-dimensional modes of MOCASSIN are consistent with each other. The small differences that do exist can be entirely attributed to the coarseness of the grids used for the three-dimensional calculations. The aim of the benchmarking described in this work is to assess the reliability of MOCASSIN in its fully *three-dimensional* mode. For this reason, the one-dimensional mode results will not be included in the following performance analysis. Moreover, the inclusion of two sets of results from what is, essentially, the same code would introduce a bias in the median and isolation factor calculations described below. Finally, to avoid any confusion, any mention of MOCASSIN throughout the rest of this paper refers to the fully three-dimensional version of the code, unless otherwise stated.

Figs 1 and 2 show the electron temperatures (top panels), and the fractional ionic abundances of oxygen (middle panels) and carbon (bottom panels) for the four benchmark cases analysed. The ionic abundances in every cell in the ionized region are plotted against radial distance from the star. These plots are interesting not only because they provide a clear picture of the overall temperature and ionization structure of each model, but also because from the scatter of the data points one can estimate the accuracy of the final results. (Note that such plots are only meaningful in the spherically symmetric case.)

Four benchmark model nebulae were computed, two H II regions and two planetary nebulae. These benchmarks were designed to be

**Figure 1.** Electron temperature (top panels), and the fractional ionic abundances of oxygen (middle panels) and carbon (bottom panels), as a function of nebular radius, for the H II region benchmark cases HII40 (left-hand panels) and HII20 (right-hand panels).

uncomplicated yet to test different aspects of the modelling (see Ferland et al. 1995). The nebulae are homogeneous in density and, for simplicity, blackbodies are used as the ionizing sources instead of model stellar atmospheres.

Following the analysis of Péquignot (see Péquignot et al. 2001), isolation factors, $if$, were computed for each predicted quantity in each case study. These are defined as the ratio of the largest to the

penultimate largest value of a given output quantity or the ratio of the penultimate smallest value to the smallest value. These ratios are computed with the intention to identify aberrant values. A large $if$ can be attributed to a number of factors, but often these can be attributed to a difference in the atomic data used by each modeller. A list of the number of $if$ larger than 1.01, 1.03, 1.10, 1.30 and 2.00 is given in Table 8, for each benchmark. After analysing the
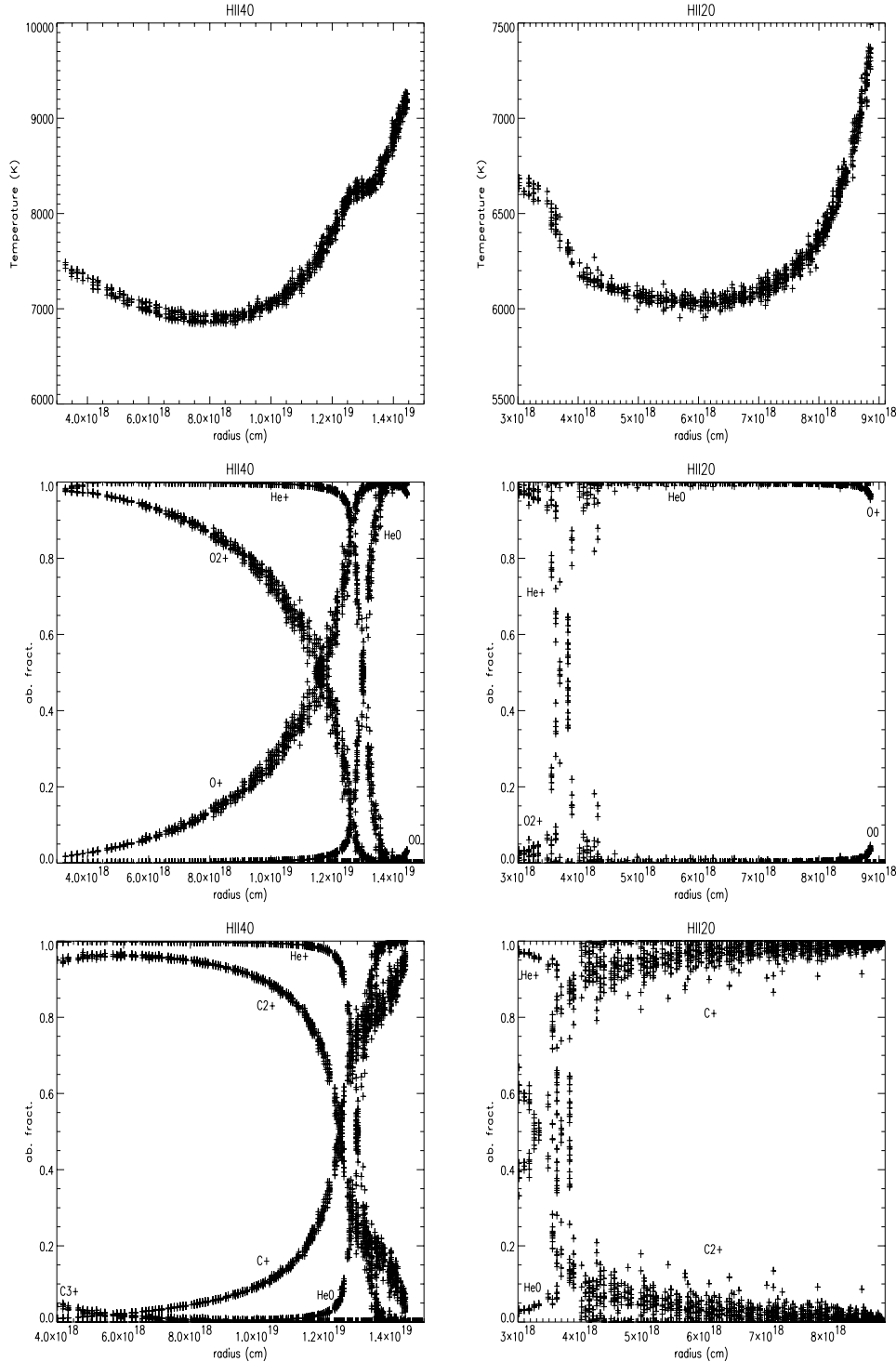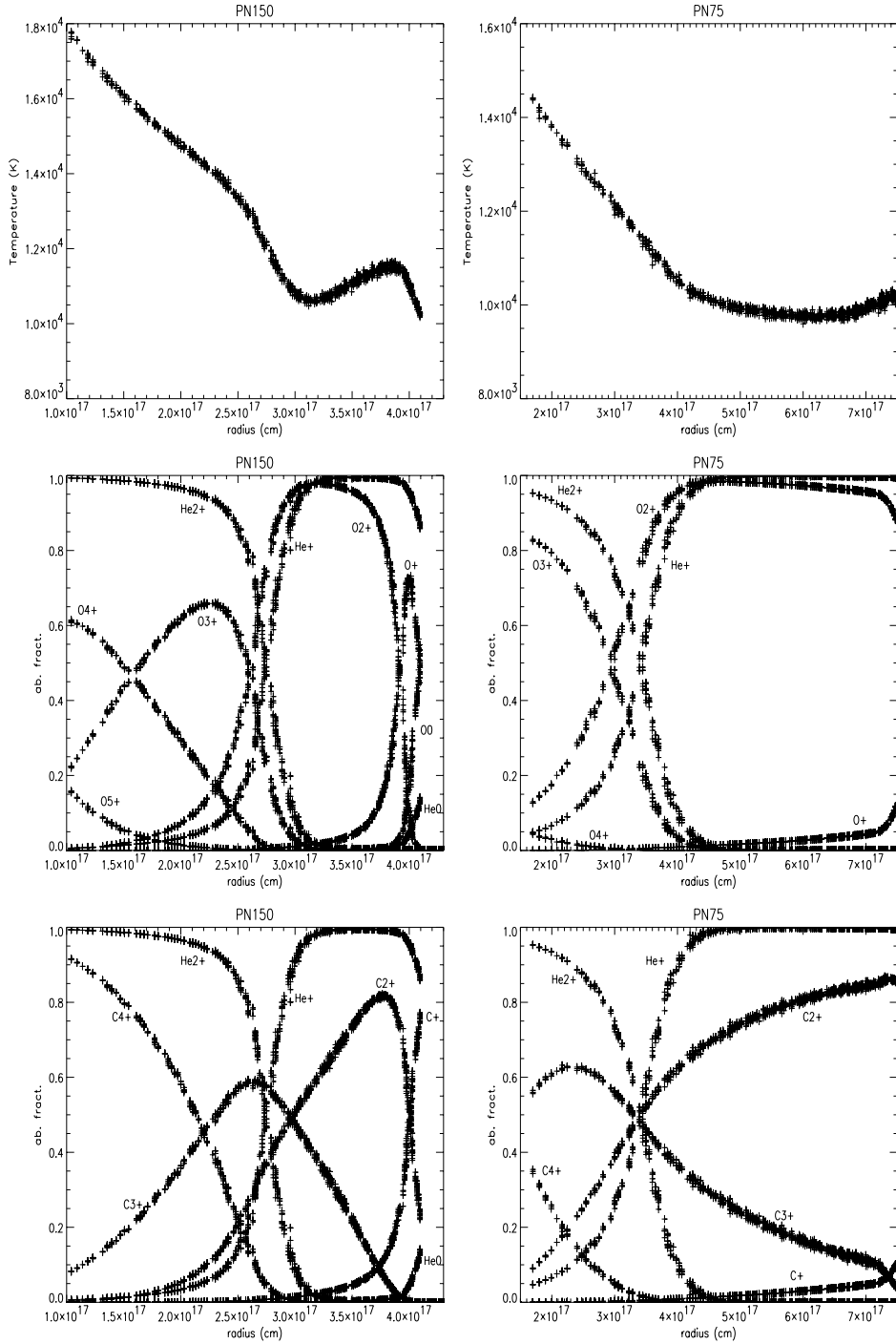
**Figure 2.** Electron temperature (top panels), and the fractional ionic abundances of oxygen (middle panels) and carbon (bottom panels), as a function of nebular radius, for the planetary nebula benchmark cases PN150 (left-hand panels) and PN75 (right-hand panels).

benchmark results obtained by all the modellers who participated in the Lexington workshop, Péquignot et al. (2001) suggested that an isolation factor larger than 1.30 is indicative of a significant departure and a possible problem. A large number of occurrences of *if* > 1.30 should either have an acceptable explanation or lead to corrections to the code.

The number of results not predicted by any given code is listed in the 'No pred.' rows of Table 8. Péquignot et al. (2001) also noted, in the proceedings of the 2000 November Lexington meeting, that

the lack of a prediction for a particular observable may simply reflect a lack of interest by the modeller in it; on the other hand, a frequent occurrence of 'No pred.' may also indicate limitations in the predictive power of a given code.

As argued by Péquignot et al. (2001), a large error can be introduced when the average over a small sample containing a number of aberrant values is taken. In order to minimize this error, median values are calculated instead of averages and these are given for each observable listed in Tables 4–7, in the column labelled 'Med'.

**Table 2.** Summary of the number of energy packets needed for >50 per cent and >95 per cent convergence (see text for explanation) for each of the benchmark cases.

| Case | $H^0$ | $\tau_{edge}$ $He^0$ | $He^+$ | $n_x \times n_y \times n_z$ | $N_{packets}$ >50% | >95% |
|------|-------|---------|--------|----------------------------|--------|--------|
| HII40 | 4.79 | 1.15 | 177.8 | $13 \times 13 \times 13$ | $5 \times 10^5$ | $5 \times 10^6$ |
| HII20 | 2.95 | 1.13 | 91.2 | $13 \times 13 \times 13$ | $5 \times 10^6$ | $5 \times 10^7$ |
| PN150 | 34.0 | 6.87 | 57.9 | $13 \times 13 \times 13$ | $3 \times 10^5$ | $3 \times 10^6$ |
| PN75 | 1.16 | 0.24 | 31.5 | $13 \times 13 \times 13$ | $4 \times 10^5$ | $4 \times 10^6$ |

**Table 3.** Deviation (per cent) of the Monte Carlo method from the formal solution for the prediction of some significant line fluxes in the benchmark models.

| Line | HII40 | HII20 | PN150 | PN75 |
|------|-------|-------|-------|------|
| H$\beta$ | 2.7 | 9.5 | 5.8 | 2.8 |
| He I 5876 Å | 5.2 | 6.3 | 0.96 | 4.5 |
| [N II] 6584 Å | 7.6 | 4.9 | 8.5 | 4.8 |
| [O II] 5007 Å | 3.1 | 12.0 | 4.0 | 1.1 |
| [S III] 9532 Å | 5.8 | 5.0 | 2.0 | 2.0 |

The medians are calculated to the precision shown in Tables 4–7. Table 9 lists the number of median values scored by each code for each benchmark, i.e. the number of times the code was the closest to the median value. When a median value is shared by two or more codes, the score is given to each one; therefore, the sum of the median values scored by all the codes is higher than the number of observables (the column labelled 'Total' in Table 9).

### 3.1 Sampling requirements

Table 2 lists the optical depths at the ionization threshold frequencies for $H^0$, $He^0$ and $He^+$, at the outer edge of the grids, for the four benchmark models analysed here. For each model, the number of grid points is also given (column 5), together with the number of energy packets used, $N_{packets}$, according to the two-step strategy described above, first to achieve convergence in 50–60 per cent of the total number of grid cells (>50 per cent, column 6) and then to achieve total convergence (>95 per cent, column 7). Table 2 shows that the softer the ionizing radiation field, the larger the number of energy packets required to achieve a given degree of convergence. The reason for this effect is that in a softer radiation field case the number of energy packets emitted at wavelengths shorter than the Lyman limit will be less than in the case of a harder radiation field. A larger total number of energy packets then needs to be used in order to obtain a number of ionizing photons adequate to sample the nebula properly. The aim of Table 2 is merely to provide some general guidelines for selecting the appropriate number of energy packets for a particular simulation; however, as stated before, the optimum number should be determined for each given model, particularly in non-spherically symmetric cases.

### 3.2 Benchmark results

The Lexington/Meudon Standard H II region model (HII40) was the first benchmark to be run, and some very preliminary results have already been presented, at the 2000 November Lexington meeting (Ercolano 2001; Péquignot et al. 2001). However, those results were produced when MOCASSIN was still under development and should therefore only be considered as a snapshot of the code at that particular stage. The code has evolved considerably since the 2000 November Lexington meeting, and the newer results are presented in this section (see Tables 4–7).

Table 3 shows the results of a comparison between the line fluxes obtained by MOCASSIN using the formal solution method and those obtained using the Monte Carlo method (see Section 2.8) for some of the more significant lines in the benchmark cases. It is clear that the results shown agree well; however, as expected, larger discrepancies were found for the weaker lines, whose lower numbers of energy packets yield lower-accuracy statistics.

#### 3.2.1 The HII40 benchmark

These benchmark case results are shown in Table 4. MOCASSIN scored eight $if > 1.01$ for the HII40 benchmark model (Table 8); only three of these, however, had values greater than 1.3. Amongst these, $if > 1.10$ are obtained for [O III] 5007+4959 Å ($if = 1.18$) and [O III] 4363 Å ($if = 1.45$); the ratio of these lines is often used as a temperature diagnostic (see, for example, Osterbrock 1989 pages 119–125). MOCASSIN predicts $(j_{\lambda 4959} + j_{\lambda 5007})/j_{\lambda 4363} = 745.4$, which is higher than the value obtained by the other codes. In fact the median value obtained for the ratio of these line fluxes by the other codes is 589.2. This is fully consistent with MOCASSIN predicting a slightly lower temperature ($if = 1.027$) for this benchmark than do the other codes.

Finally, the number of median values obtained for this benchmark case is 10, which compares very well with the other codes' median scores, ranging from three to 10 (see Table 9).

#### 3.2.2 The HII20 benchmark

These benchmark case results are shown in Table 5. MOCASSIN scored seven $if$ for the low-excitation H II region (HII20) benchmark model. None of these, however, has a value greater than 1.3. As in the HII40 benchmark case, the mean temperature, weighted by $N_p N_e$, predicted by MOCASSIN for this model is also slightly lower ($if = 1.034$) than the other models' predictions.

Five median values were obtained by MOCASSIN for this benchmark case, while the other codes scored between three and 11 (see Table 9).

#### 3.2.3 The PN150 benchmark

These benchmark case results are shown in Table 6. The optically thick high-excitation planetary nebula (PN150) is the most demanding of the benchmark cases in terms of physical processes and atomic data required. MOCASSIN's score for this model was very good (Table 8), obtaining only six $if$, with none of those being higher than 1.3 and only one slightly higher than 1.1 (C II 1335 Å, $if = 1.13$). As has already been discussed by Péquignot et al. (2001), there seems to be a dichotomy between the GF, HN and DP models (and, now, also the BE model) on the one hand, and the TK, PH and RS models on the other. The former group obtained very few $if$ larger than 1.1, indicative of a tighter agreement. This coherence can probably be attributed to a more recent updating of atomic data and a more careful treatment of the diffuse radiation field transfer. These four codes also obtained a larger H$\beta$ flux for this model, which can probably be ascribed to secondary photons from heavy ions. PH is the only classical code here with a fully iterative spherically symmetric radiative transfer treatment (since RR only computed H II regions); this could also be the reason for the relatively larger number of $if$ scored by the PH code for this model.

**Table 4.** Lexington 2000 standard H II region (HII40) benchmark case results.[a]

| Line | Median | GF | HN | DP | TK | PH | RS | RR | BE 3D | BE 1D |
|------|--------|-----|-----|-----|-----|-----|-----|-----|------|------|
| $H\beta/10^{37}$ erg s$^{-1}$ | 2.05 | 2.06 | 2.02 | 2.02 | 2.10 | 2.05 | 2.07 | 2.05 | 2.02 | 2.10 |
| $H\beta$ 4861 | – | 1.00 | 1.00 | 1.00 | 1.00 | 1.00 | 1.00 | 1.00 | 1.00 | 1.00 |
| He I 5876 | 0.116 | 0.119 | 0.112 | 0.113 | 0.116 | 0.118 | 0.116 | – | 0.114 | 0.112 |
| C II] 2325+ | 0.144 | 0.157 | 0.141 | 0.139 | 0.110 | 0.166 | 0.096 | 0.178 | 0.148 | 0.126 |
| C II 1335 | 0.082 | 0.100 | 0.078 | 0.094 | 0.004 | 0.085 | 0.010 | – | 0.082 | 0.084 |
| C III] 1907+1909 | 0.070 | 0.071 | 0.076 | 0.069 | 0.091 | 0.060 | 0.066 | 0.074 | 0.041 | 0.041 |
| [N II] 122 μm | 0.034 | 0.027 | 0.037 | 0.034 | – | 0.032 | 0.035 | 0.030 | 0.036 | 0.034 |
| [N II] 6584+6548 | 0.730 | 0.669 | 0.817 | 0.725 | 0.69 | 0.736 | 0.723 | 0.807 | 0.852 | 0.786 |
| [N II] 5755 | 0.0054 | 0.0050 | 0.0054 | 0.0050 | – | 0.0064 | 0.0050 | 0.0068 | 0.0061 | 0.0054 |
| [N III] 57.3 μm | 0.292 | 0.306 | 0.261 | 0.311 | – | 0.292 | 0.273 | 0.301 | 0.223 | 0.229 |
| [O I] 6300+6363 | 0.0086 | 0.0094 | 0.0086 | 0.0088 | 0.012 | 0.0059 | 0.0070 | – | 0.0065 | 0.0080 |
| [O II] 7320+7330 | 0.029 | 0.029 | 0.030 | 0.031 | 0.023 | 0.032 | 0.024 | 0.036 | 0.025 | 0.022 |
| [O II] 3726+3729 | 2.03 | 1.94 | 2.17 | 2.12 | 1.6 | 2.19 | 1.88 | 2.26 | 1.92 | 1.75 |
| [O III] 51.8 μm | 1.06 | 1.23 | 1.04 | 1.03 | 0.99 | 1.09 | 1.06 | 1.08 | 1.06 | 1.09 |
| [O III] 88.3 μm | 1.22 | 1.12 | 1.06 | 1.23 | 1.18 | 1.25 | 1.23 | 1.25 | 1.22 | 1.26 |
| [O III] 5007+4959 | 2.18 | 2.21 | 2.38 | 2.20 | 3.27 | 1.93 | 2.17 | 2.08 | 1.64 | 1.70 |
| [O III] 4363 | 0.0037 | 0.0035 | 0.0046 | 0.0041 | 0.0070 | 0.0032 | 0.0040 | 0.0035 | 0.0022 | 0.0023 |
| [O IV] 25.9 μm | 0.0010 | 0.0010 | 0.0010 | 0.0010 | 0.0013 | 0.0013 | 0.0010 | – | 0.0010 | 0.0010 |
| [Ne II] 12.8 μm | 0.195 | 0.177 | 0.195 | 0.192 | – | 0.181 | 0.217 | 0.196 | 0.212 | 0.209 |
| [Ne III] 15.5 μm | 0.322 | 0.294 | 0.264 | 0.270 | 0.35 | 0.429 | 0.350 | 0.417 | 0.267 | 0.269 |
| [Ne III] 3869+3968 | 0.085 | 0.084 | 0.087 | 0.071 | 0.092 | 0.087 | 0.083 | 0.086 | 0.053 | 0.055 |
| [S II] 6716+6731 | 0.147 | 0.137 | 0.166 | 0.153 | 0.315 | 0.155 | 0.133 | 0.130 | 0.141 | 0.138 |
| [S II] 4068+4076 | 0.0080 | 0.0093 | 0.0090 | 0.0100 | 0.026 | 0.0070 | 0.005 | 0.0060 | 0.0060 | 0.0057 |
| [S III] 18.7 μm | 0.577 | 0.627 | 0.750 | 0.726 | 0.535 | 0.556 | 0.567 | 0.580 | 0.574 | 0.569 |
| [S III] 33.6 μm | 0.937 | 1.24 | 1.43 | 1.36 | 0.86 | 0.892 | 0.910 | 0.936 | 0.938 | 0.932 |
| [S III] 9532+9069 | 1.22 | 1.13 | 1.19 | 1.16 | 1.25 | 1.23 | 1.25 | 1.28 | 1.21 | 1.19 |
| [S IV] 10.5 μm | 0.359 | 0.176 | 0.152 | 0.185 | 0.56 | 0.416 | 0.388 | 0.330 | 0.533 | 0.539 |
| $10^3\Delta$(BC 3645)/Å | 5.00 | 4.88 | – | 4.95 | – | 5.00 | 5.70 | – | 5.47 | 5.45 |
| $T_{inner}$/K | 7653 | 7719 | 7668 | 7663 | 8318 | 7440 | 7644 | 7399 | 7370 | 7480 |
| $\langle T[N_p\,N_e]\rangle$/K | 8026 | 7940 | 7936 | 8082 | 8199 | 8030 | 8022 | 8060 | 7720 | 7722 |
| $R_{out}/10^{19}$ cm | 1.46 | 1.46 | 1.46 | 1.46 | 1.45 | 1.46 | 1.47 | 1.46 | 1.46 | 1.49 |
| $\langle He^+\rangle/\langle H^+\rangle$ | 0.767 | 0.787 | 0.727 | 0.754 | 0.77 | 0.764 | 0.804 | 0.829 | 0.715 | 0.686 |

[a] GF: G. Ferland's cloudy; HN: H. Netzer's ion; DP: D. Péquignot's nebu; TK: T. Kallman's xstar; PH: J. P. Harrington's code; RS: R. Sutherland's mappings; RR: R. Rubin's nebula; BE: B. Ercolano's MOCASSIN.

The score for median values obtained by MOCASSIN for the PN150 optically thick planetary nebula is extremely good, obtaining the highest value of 15 medians, above the other codes, which obtained between two and 13 (see Table 9).

### 3.2.4 The PN75 benchmark

These benchmark case results are shown in Table 7. The optically thin planetary nebula (PN75) benchmark model is not a radiation-bounded case, but a matter-bounded one and, in fact, the outer radius is given as an input parameter to all codes and fixed at $7.5 \times 10^{19}$ cm. For this reason, for this particular model there is not a straightforward *conservation law* for the absolute flux of $H\beta$. This can be used to explain, in part at least, the relatively poor scores of the GF code for low $if$ (Table 8), since, for one reason or another, its predicted $H\beta$ flux deviated somewhat from the median value, thus shifting all the other line intensities, given in $H\beta$ units. The PH code also obtained an $H\beta$ flux which deviated from the median value; in this case, however, the number of total $if$ stayed low (=5) and no $if > 1.30$ was obtained. MOCASSIN, however, obtained a low number of $if$ for this relatively difficult case, scoring nine $if$ in total, with none of those having a value greater than 1.30.

MOCASSIN obtained a score of 13 median values for this benchmark case, which compares well with the scores obtained by the other codes for this benchmark, ranging from eight to 19 median values (see Table 9).

## 4 DISCUSSION

The overall performance of MOCASSIN for the four benchmarks was very satisfactory, as shown by Table 8. The results obtained from the one-dimensional mode of MOCASSIN are, in general, in very good agreement with those obtained using the fully three-dimensional MOCASSIN models. One noticeable difference, common to all four benchmarks, is that the kinetic temperature at the illuminated inner edge of the nebula, $T_{inner}$, is higher for the one-dimensional MOCASSIN results and closer to the values obtained by the other one-dimensional codes included in the comparison. This is an obvious effect caused by the coarseness of the three-dimensional grid: since all the physical properties of the gas are constant within each volume element, then the electron temperature of a given cell will be mainly representative of the kinetic temperature at its centre. From this, it naturally follows that the coarser the grid, and the larger the cells, then the further the kinetic temperature at the centres of the cells adjacent to the inner radius will be from the true value at the inner radius.

The electron temperatures, $\langle T[N_p N_e]\rangle$ and $T_{inner}$, predicted by MOCASSIN for the Lexington benchmark models tend, in particular

**Table 5.** Lexington 2000 low-excitation H II region (HII20) benchmark case results.[a]

| Line | Med | GF | HN | DP | TK | PH | RS | RR | BE 3D | BE 1D |
|---|---|---|---|---|---|---|---|---|---|---|
| $H\beta/10^{36}$ erg s$^{-1}$ | 4.91 | 4.85 | 4.85 | 4.83 | 4.9 | 4.93 | 5.04 | 4.89 | 4.97 | 5.09 |
| $H\beta$ 4861 | – | 1.00 | 1.00 | 1.00 | 1.00 | 1.00 | 1.00 | 1.00 | 1.00 | 1.00 |
| He I 5876 | 0.0074 | 0.0072 | 0.008 | 0.0073 | 0.008 | 0.0074 | 0.0110 | – | 0.0065 | 0.0074 |
| C II] 2325+ | 0.046 | 0.054 | 0.047 | 0.046 | 0.040 | 0.060 | 0.038 | 0.063 | 0.042 | 0.031 |
| [N II] 122 μm | 0.071 | 0.068 | – | 0.072 | 0.007 | 0.072 | 0.071 | 0.071 | 0.071 | 0.070 |
| [N II] 6584+6548 | 0.823 | 0.745 | 0.786 | 0.785 | 0.925 | 0.843 | 0.803 | 0.915 | 0.846 | 0.771 |
| [N II] 5755 | 0.0028 | 0.0028 | 0.0024 | 0.0023 | 0.0029 | 0.0033 | 0.0030 | 0.0033 | 0.0025 | 0.0021 |
| [N III] 57.3 μm | 0.0030 | 0.0040 | 0.0030 | 0.0032 | 0.0047 | 0.0031 | 0.0020 | 0.0022 | 0.0019 | 0.0032 |
| [O I] 6300+6363 | 0.0060 | 0.0080 | 0.0060 | 0.0063 | 0.0059 | 0.0047 | 0.0050 | – | 0.0088 | 0.0015 |
| [O I] 7320+7330 | 0.0086 | 0.0087 | 0.0085 | 0.0089 | 0.0037 | 0.0103 | 0.0080 | 0.0100 | 0.0064 | 0.0051 |
| [O II] 3726+3729 | 1.09 | 1.01 | 1.13 | 1.10 | 1.04 | 1.22 | 1.08 | 1.17 | 0.909 | 0.801 |
| [O III] 51.8 μm | 0.0012 | 0.0014 | 0.0012 | 0.0012 | 0.0016 | 0.0013 | 0.0010 | 0.0008 | 0.0010 | 0.0011 |
| [O III] 88.3 μm | 0.0014 | 0.0016 | 0.0014 | 0.0014 | 0.0024 | 0.0014 | 0.0010 | 0.0009 | 0.0012 | 0.0013 |
| [O III] 5007+4959 | 0.0014 | 0.0021 | 0.0016 | 0.0015 | 0.0024 | 0.0014 | 0.0010 | 0.0010 | 0.0011 | 0.0012 |
| [Ne II] 12.8 μm | 0.273 | 0.264 | 0.267 | 0.276 | 0.27 | 0.271 | 0.286 | 0.290 | 0.295 | 0.296 |
| [S II] 6716+6731 | 0.489 | 0.499 | 0.473 | 0.459 | 1.02 | 0.555 | 0.435 | 0.492 | 0.486 | 0.345 |
| [S II] 4068+4076 | 0.017 | 0.022 | 0.017 | 0.020 | 0.052 | 0.017 | 0.012 | 0.015 | 0.013 | 0.0082 |
| [S III] 18.7 μm | 0.386 | 0.445 | 0.460 | 0.441 | 0.34 | 0.365 | 0.398 | 0.374 | 0.371 | 0.413 |
| [S III] 33.6 μm | 0.658 | 0.912 | 0.928 | 0.845 | 0.58 | 0.601 | 0.655 | 0.622 | 0.630 | 0.702 |
| [S III] 9532+9069 | 0.537 | 0.501 | 0.480 | 0.465 | 0.56 | 0.549 | 0.604 | 0.551 | 0.526 | 0.582 |
| $10^3 \Delta$(BC 3645)/Å | 5.57 | 5.54 | – | 5.62 | – | 5.57 | 5.50 | – | 6.18 | 6.15 |
| $T_{inner}$/K | 6765 | 7224 | 6815 | 6789 | 6607 | 6742 | 6900 | 6708 | 6562 | 6662 |
| $\langle T[N_p\,N_e]\rangle$/K | 6662 | 6680 | 6650 | 6626 | 6662 | 6749 | 6663 | 6679 | 6402 | 6287 |
| $R_{out}/10^{18}$ cm | 8.89 | 8.89 | 8.88 | 8.88 | 8.7 | 8.95 | 9.01 | 8.92 | 8.89 | 8.92 |
| $\langle He^+\rangle/\langle H^+\rangle$ | 0.048 | 0.048 | 0.051 | 0.049 | 0.048 | 0.044 | 0.077 | 0.034 | 0.041 | 0.048 |

[a] GF: G. Ferland's cloudy; HN: H. Netzer's ion; DP: D. Péquignot's nebu; TK: T. Kallman's xstar; PH: J. P. Harrington's code; RS: R. Sutherland's mappings; RR: R. Rubin's nebula; BE: B. Ercolano's MOCASSIN.

in the H II region cases, towards the lower limit of the scatter. In the case of $T_{inner}$, this seems to be a characteristic of all codes using an exact treatment for the radiative transfer. As noted by Péquignot et al. (2001), the kinetic temperatures calculated by codes with exact transfer tend to be lower in the innermost layers of the nebula, as the ionizing radiation field there is softer. Only two codes in the Lexington benchmarks treated the radiative transfer exactly, namely Rubin's NEBULA (RR) and the Harrington code (PH) and, in fact, MOCASSIN's results for the kinetic temperatures generally agree better with those two codes' predictions. For the standard H II region benchmark (HII40), MOCASSIN's kinetic temperature at the inner edge of the nebula, $T_{inner}$, agrees extremely well with the predictions of the RR and PH codes. Similar results are obtained for the low-excitation H II region benchmark (HII20), where, again, MOCASSIN's $T_{inner}$ agrees with the results of PH and RR. In both H II regions benchmark cases, however, MOCASSIN predicted a value that was about 250 K lower than the median for $\langle T[N_p N_e]\rangle$, obtaining an $if = 1.027$ for the HII40 case and $if = 1.034$ for the HII20 case. The cause of this small discrepancy is not clear to us.

Unfortunately, Rubin's code NEBULA was not designed to treat planetary nebulae and, therefore, the only exact one-dimensional radiative transfer code available for the optically thick planetary nebula (PN150) and the optically thin planetary nebula (PN75) benchmarks is the Harrington code (PH). For PN150, MOCASSIN's $T_{inner}$ is in reasonable agreement with PH's prediction, particularly if the prediction from the one-dimensional MOCASSIN run is considered, since, as discussed earlier, this represents a measurement of the temperature taken closer to the inner edge of the nebula. The MOCASSIN result for $\langle T[N_p N_e]\rangle$ is within the scatter and, in particular, BE and PH agree very well for this observable. Note that only HN and TK

obtain higher temperatures for this model; moreover, the TK computation was carried out with a new code, still under development, primarily designed for X-ray studies. That code could not treat the diffuse radiation field, leading to problems for the hard radiation field cases, such as PN150. Finally, for the PN75 benchmark planetary nebula, MOCASSIN's $T_{inner}$ is within the scatter (the prediction from the one-dimensional model is actually at the higher limit of it) and in reasonable agreement with PH's prediction; the result for $\langle T[N_p N_e]\rangle$ is also within the scatter and is in very good agreement with the prediction of the PH code. Once again, only HN predicts a higher value for this quantity, while TK's results for this model are not available.

The models presented in this chapter were all run using a 13 × 13 × 13 grid and, since they are all spherically symmetric, the ionizing source was placed in a corner of the grid. The number of energy packets used to sample the grids and bring them to convergence varied from three to five million. As has already been discussed, the accuracy of the results depends both on the spatial sampling (i.e. the number of grid cells) and on the number of energy packets used. It is clear, however, that the latter also depends on the number of points to be sampled. So if, for example, in a given simulation the number of grid cells is increased from $n_x \times n_y \times n_z$ to $n'_x \times n'_y \times n'_z$, then the number of energy packets used must also be increased from $N_{packets}$ to

$$N'_{packets} = \frac{n'_x \times n'_y \times n'_z}{n_x \times n_y \times n_z} N_{packets}.$$

However, for these relatively simple cases, the three-dimensional grid specified above was found to be sufficient to produce acceptable results. In fact, since the benchmark models are spherically

**Table 6.** Lexington 2000 thick planetary nebula (PN150) benchmark case results.[a]

| Line | Med | GF | HN | DP | TK | PH | RS | BE 3D | BE 1D |
|---|---|---|---|---|---|---|---|---|---|
| $H_\beta/10^{35}$ erg s$^{-1}$ | 2.79 | 2.86 | 2.83 | 2.84 | 2.47 | 2.68 | 2.64 | 2.79 | 2.89 |
| $H_\beta$ 4861 | – | 1.00 | 1.00 | 1.00 | 1.00 | 1.00 | 1.00 | 1.00 | 1.00 |
| He I 5876 | 0.104 | 0.110 | 0.129 | 0.118 | 0.096 | 0.096 | 0.095 | 0.104 | 1.06 |
| He II 4686 | 0.328 | 0.324 | 0.304 | 0.305 | 0.341 | 0.333 | – | 0.333 | 0.320 |
| C II] 2325+ | 0.293 | 0.277 | 0.277 | 0.293 | 0.346 | 0.450 | 0.141 | 0.339 | 0.330 |
| C II 1335 | 0.119 | 0.121 | 0.116 | 0.130 | – | 0.119 | – | 0.103 | 0.104 |
| C III] 1907+1909 | 0.174 | 1.68 | 1.74 | 1.86 | 1.69 | 1.74 | 1.89 | 1.72 | 1.71 |
| C IV 1549+ | 2.16 | 2.14 | 2.43 | 2.16 | 0.154 | 2.09 | 3.12 | 2.71 | 2.65 |
| [N I] 5200+5198 | 0.012 | 0.013 | 0.022 | 0.010 | – | 0.020 | 0.005 | 0.0067 | 0.012 |
| [N II] 6584+6548 | 1.17 | 1.15 | 1.16 | 1.18 | 1.01 | 1.35 | 1.17 | 1.43 | 1.37 |
| [N II] 5755 | 0.017 | 0.017 | 0.016 | 0.017 | 0.020 | 0.023 | 0.016 | 0.022 | 0.0021 |
| N III] 1749+ | 0.111 | 0.106 | 0.109 | 0.132 | 0.184 | 0.139 | 0.091 | 0.111 | 0.110 |
| [N III] 57.3 μm | 0.129 | 0.129 | 0.133 | 0.134 | 0.12 | 0.135 | 0.126 | 0.120 | 0.122 |
| N IV] 1487+ | 0.168 | 0.199 | 0.178 | 0.192 | 0.154 | 0.141 | 0.168 | 0.162 | 0.159 |
| N V 1240+ | 0.147 | 0.147 | 0.159 | 0.154 | 0.055 | 0.107 | 0.248 | 0.147 | 0.145 |
| [O I] 63.1 μm | 0.020 | 0.024 | 0.017 | 0.025 | – | 0.0072 | 0.049 | 0.010 | 0.011 |
| [O I] 6300+6363 | 0.135 | 0.144 | 0.126 | 0.135 | 0.245 | 0.104 | 0.101 | 0.163 | 0.153 |
| [O II] 3726+3729 | 2.11 | 2.03 | 1.96 | 2.32 | 2.11 | 2.66 | 1.75 | 2.24 | 2.25 |
| [O III] 51.8 μm | 1.39 | 1.30 | 1.45 | 1.42 | 0.954 | 1.39 | 1.28 | 1.50 | 1.52 |
| [O III] 88.3 μm | 0.274 | 0.261 | 0.292 | 0.291 | 0.27 | 0.274 | 0.252 | 0.296 | 0.299 |
| [O III] 5007+4959 | 21.4 | 21.4 | 22.2 | 21.1 | 26.0 | 20.8 | 16.8 | 22.63 | 22.52 |
| [O III] 4363 | 0.155 | 0.152 | 0.151 | 0.156 | 0.249 | 0.155 | 0.109 | 0.169 | 0.166 |
| [O IV] 25.9 μm | 3.78 | 3.45 | 3.16 | 3.78 | 3.95 | 4.20 | 4.05 | 3.68 | 3.60 |
| O IV] 1403+ | 2.30 | 0.183 | 0.236 | 0.324 | 0.357 | 0.225 | – | 0.203 | 0.201 |
| O V] 1218+ | 0.169 | 0.165 | 0.189 | 0.170 | 0.142 | 0.097 | 0.213 | 0.169 | 0.168 |
| O VI 1034+ | 0.025 | 0.028 | 0.026 | 0.022 | 0.026 | 0.014 | – | 0.025 | 0.026 |
| [Ne II] 12.8 μm | 0.030 | 0.028 | 0.032 | 0.030 | 0.020 | 0.027 | 0.043 | 0.030 | 0.031 |
| [Ne III] 15.5 μm | 1.97 | 1.88 | 1.97 | 1.92 | 1.73 | 2.76 | 2.71 | 2.02 | 2.03 |
| [Ne III] 3869+3968 | 2.63 | 2.64 | 2.32 | 2.25 | 2.86 | 3.04 | 2.56 | 2.63 | 2.61 |
| [Ne IV] 2423+ | 0.723 | 0.707 | 0.712 | 0.785 | 1.13 | 0.723 | 0.832 | 0.749 | 0.741 |
| [Ne V] 3426+3346 | 0.692 | 0.721 | 0.706 | 0.661 | 1.07 | 0.583 | 0.591 | 0.692 | 0.687 |
| [Ne V] 24.2 μm | 0.980 | 0.997 | 0.98 | 0.928 | 1.96 | 0.936 | 0.195 | 1.007 | 0.997 |
| [Ne VI] 7.63 μm | 0.076 | 0.107 | 0.075 | 0.077 | 0.692 | 0.011 | – | 0.050 | 0.051 |
| Mg II 2798+ | 1.22 | 2.22 | 2.10 | 1.22 | 0.023 | 0.555 | 0.863 | 2.32 | 2.32 |
| [Mg IV] 4.49 μm | 0.111 | 0.121 | 0.111 | 0.107 | 0.13 | 0.042 | 0.115 | 0.111 | 0.109 |
| [Mg V] 5.61 μm | 0.144 | 0.070 | 0.132 | 0.162 | 0.18 | 0.066 | – | 0.156 | 0.156 |
| [Si II] 34.8 μm | 0.168 | 0.155 | 0.168 | 0.159 | 0.263 | 0.253 | 0.130 | 0.250 | 0.263 |
| Si II] 2335+ | 0.159 | 0.160 | 0.155 | 0.158 | 0.20 | – | 0.127 | 0.160 | 0.164 |
| Si III] 1892+ | 0.382 | 0.446 | 0.547 | 0.475 | 0.321 | 0.382 | 0.083 | 0.325 | 0.316 |
| Si IV 1397+ | 0.172 | 0.183 | 0.218 | 0.169 | 0.015 | 0.172 | 0.122 | 0.214 | 0.207 |
| [S II] 6716+6731 | 0.370 | 0.359 | 0.37 | 0.399 | 0.415 | 0.451 | 0.322 | 0.357 | 0.370 |
| [S II] 4069+4076 | 0.077 | 0.073 | 0.078 | 0.086 | 0.19 | 0.077 | 0.050 | 0.064 | 0.063 |
| [S III] 18.7 μm | 0.578 | 0.713 | 0.788 | 0.728 | 0.15 | 0.488 | 0.578 | 0.495 | 0.505 |
| [S III] 33.6 μm | 0.240 | 0.281 | 0.289 | 0.268 | 0.06 | 0.206 | 0.240 | 0.210 | 0.214 |
| [S III] 9532+9069 | 1.96 | 2.07 | 2.07 | 1.96 | 0.61 | 1.90 | 2.04 | 1.89 | 1.92 |
| [S IV] 10.5 μm | 2.22 | 2.09 | 1.65 | 1.76 | 2.59 | 2.22 | 2.25 | 2.25 | 2.22 |
| $T_{inner}$/K | 18100 | 18120 | 17950 | 18100 | 19050 | 17360 | 19100 | 16670 | 17703 |
| $\langle T[N_p N_e]\rangle$/K | 12110 | 12080 | 13410 | 12060 | 13420 | 12110 | 11890 | 12150 | 12108 |
| $R_{out}/10^{17}$ cm | 4.04 | 4.04 | 3.90 | 4.11 | 4.07 | 4.04 | 3.98 | 4.11 | 4.19 |
| $\langle He^+\rangle/\langle H^+\rangle$ | 0.704 | 0.702 | 0.726 | 0.714 | 0.79 | 0.696 | 0.652 | 0.702 | 0.711 |

[a]GF: G. Ferland's cloudy; HN: H. Netzer's ion; DP: D. Péquignot's nebu; TK: T. Kallman's xstar; PH: J. P. Harrington's code; RS: R. Sutherland's mappings; BE: B. Ercolano's MOCASSIN.

symmetric, then, although the number of sampling points along each orthogonal axis is only 13, this is the equivalent of a one-dimensional code with 273 radial points, which is the number of different values of $r$ given by all the $(x, y, z)$ combinations. This is clearly demonstrated in Figs 1 and 2, where the number of data points and the spacing between them shows that the spatial sampling is indeed appropriate. The plots also show that the number of energy packets used in the simulations was sufficient, since the scatter of the ordinate values for a given $r$, which is essentially a measure of the error bars, is very small. The largest scatter was obtained in the plots for the HII20 benchmark (Fig. 1); this is a very soft ionizing radiation field case and a larger number of energy packets is probably required in order to reduce the scatter shown and increase the accuracy of the results. For the purpose of this benchmark exercise, however, the accuracy achieved for HII20 is sufficient to produce satisfactory results.

**Table 7.** Lexington 2000 optically thin planetary nebula (PN75) benchmark case results.

| Line | Med | GF | HN | DP | PH | RS | BE 3D | BE 1D |
|---|---|---|---|---|---|---|---|---|
| $H_\beta/10^{34}$ erg s$^{-1}$ | 5.71 | 6.08 | 5.56 | 5.74 | 5.96 | 5.69 | 5.65 | 5.63 |
| $H_\beta$ 4861 | – | 1.00 | 1.00 | 1.00 | 1.00 | 1.00 | 1.00 | 1.00 |
| He I 5876 | 0.131 | 0.130 | 0.144 | 0.132 | 0.126 | 0.125 | 0.132 | 0.132 |
| He II 4686 | 0.087 | 0.085 | 0.089 | 0.087 | 0.087 | – | 0.093 | 0.094 |
| C II 2325+ | 0.039 | 0.023 | 0.047 | 0.040 | 0.044 | 0.034 | 0.038 | 0.043 |
| C II 1335 | 0.089 | 0.096 | 0.089 | 0.101 | 0.085 | – | 0.086 | 0.085 |
| C III] 1907+1909 | 0.790 | 0.584 | 0.96 | 0.882 | 0.602 | 1.00 | 0.698 | 0.709 |
| C IV 1549+ | 0.354 | 0.298 | 0.480 | 0.393 | 0.291 | 0.315 | 0.414 | 0.463 |
| [N II] 6584+6548 | 0.098 | 0.069 | 0.097 | 0.089 | 0.108 | 0.119 | 0.100 | 0.087 |
| [N II] 5755 | 0.0012 | – | 0.0011 | 0.0012 | 0.0013 | 0.0020 | 0.0011 | 0.0010 |
| N III] 1749+ | 0.043 | 0.029 | 0.059 | 0.056 | 0.038 | 0.048 | 0.038 | 0.039 |
| [N III] 57.3 μm | 0.397 | 0.371 | 0.405 | 0.404 | 0.390 | 0.405 | 0.336 | 0.334 |
| N IV] 1487+ | 0.018 | 0.019 | 0.024 | 0.020 | 0.012 | 0.011 | 0.017 | 0.020 |
| [O II] 3726+3729 | 0.262 | 0.178 | 0.262 | 0.266 | 0.262 | 0.311 | 0.234 | 0.205 |
| [O III] 5007+4959 | 11.35 | 10.1 | 13.2 | 11.7 | 10.1 | 11.8 | 11.0 | 11.1 |
| [O III] 4363 | 0.060 | 0.046 | 0.077 | 0.066 | 0.048 | 0.065 | 0.056 | 0.057 |
| [O III] 51.8 μm | 1.98 | 1.94 | 2.09 | 1.94 | 1.95 | 2.02 | 2.07 | 2.07 |
| [O III] 88.3 μm | 1.12 | 0.986 | 1.13 | 1.12 | 1.07 | 1.12 | 1.14 | 1.14 |
| [O IV] 25.9 μm | 0.814 | 0.767 | 0.741 | 0.859 | 0.821 | 0.807 | 0.894 | 0.942 |
| O IV] 1403+ | 0.013 | 0.009 | 0.015 | 0.014 | 0.093 | – | 0.013 | 0.015 |
| [Ne II] 12.8 μm | 0.012 | 0.012 | 0.012 | 0.012 | 0.012 | 0.017 | 0.013 | 0.012 |
| [Ne III] 15.5 μm | 0.948 | 0.883 | 0.95 | 0.902 | 1.32 | 1.35 | 0.946 | 0.949 |
| [Ne III] 3869+3968 | 0.872 | 0.784 | 0.948 | 0.818 | 0.919 | 1.10 | 0.826 | 0.838 |
| [Ne IV] 2423+ | 0.030 | 0.028 | 0.032 | 0.036 | 0.027 | 0.020 | 0.034 | 0.039 |
| Mg II 2798+ | 0.102 | 0.086 | 0.14 | 0.111 | 0.071 | 0.093 | 0.114 | 0.106 |
| [Mg IV] 4.49 μm | 0.0062 | 0.0021 | 0.006 | 0.0075 | 0.0065 | 0.0050 | 0.0068 | 0.0072 |
| [Si II] 34.8 μm | 0.029 | 0.025 | 0.034 | 0.025 | 0.060 | 0.004 | 0.061 | 0.052 |
| Si II 2335+ | 0.0057 | 0.0037 | 0.0078 | 0.0054 | – | 0.0010 | 0.0062 | 0.0052 |
| Si III] 1892+ | 0.104 | 0.087 | 0.16 | 0.136 | 0.101 | 0.019 | 0.107 | 0.110 |
| Si IV 1397+ | 0.017 | 0.017 | 0.023 | 0.018 | 0.013 | 0.023 | 0.016 | 0.018 |
| [S II] 6716+6731 | 0.0020 | 0.023 | 0.036 | 0.029 | 0.013 | 0.016 | 0.017 | 0.013 |
| [S II] 4069+4076 | 0.0017 | 0.0022 | 0.0034 | 0.0030 | 0.0013 | 0.0010 | 0.0012 | 0.0010 |
| [S III] 18.7 μm | 0.486 | 0.619 | 0.715 | 0.631 | 0.316 | 0.357 | 0.285 | 0.266 |
| [S III] 33.6 μm | 0.533 | 0.702 | 0.768 | 0.684 | 0.339 | 0.383 | 0.306 | 0.285 |
| [S III] 9532+9069 | 1.20 | 1.31 | 1.51 | 1.33 | 0.915 | 1.09 | 0.831 | 0.777 |
| [S IV] 10.5 μm | 1.94 | 1.71 | 1.57 | 1.72 | 2.17 | 2.33 | 2.79 | 2.87 |
| $10^3 \Delta$(BC 3645)/Å | 4.35 | 4.25 | – | 4.25 | 4.35 | 4.90 | 4.54 | 4.56 |
| $T_{inner}$/K | 14300 | 14450 | 14640 | 14680 | 14150 | 13620 | 14100 | 14990 |
| $\langle T[N_p N_e]\rangle$/K | 10425 | 9885 | 11260 | 10510 | 10340 | 10510 | 10220 | 10263 |
| $R_{out}/10^{17}$ cm | – | 7.50 | 7.50 | 7.50 | 7.50 | 7.50 | 7.50 | 7.50 |
| $\langle He^+\rangle/\langle H^+\rangle$ | 0.913 | 0.912 | 0.92 | 0.914 | 0.920 | 0.913 | 0.911 | 0.908 |
| $\tau$(1 Ryd) | 1.47 | 1.35 | 1.64 | 1.61 | 1.47 | – | 1.15 | 1.29 |

[a]GF: G. Ferland's cloudy; HN: H. Netzer's ion; DP: D. Péquignot's nebu; PH: J. P. Harrington's code; RS: R. Sutherland's mappings; BE: B. Ercolano's MOCASSIN.

## 5 CONCLUSIONS

A fully three-dimensional photoionization code, MOCASSIN, has been developed for the modelling of photoionized nebulae, using Monte Carlo techniques. The stellar and diffuse radiation fields are treated self-consistently; moreover, MOCASSIN is completely independent of the assumed nebular geometry and is therefore ideal for the study of aspherical and/or inhomogeneous nebulae, or nebulae having one or more exciting stars at non-central locations.

The code has been successfully benchmarked against established one-dimensional photoionization codes for standard spherically symmetric model nebulae (see Péquignot 1986; Ferland et al. 1995; Péquignot et al. 2001).

MOCASSIN is now ready for the application to real astronomical nebulae and it should provide an important tool for the construction of realistic nebular models. Paper II will present detailed results from the modelling of the non-spherically symmetric PN NGC 3918. Resources permitting, it is intended to make the MOCASSIN source code publicly available in the near future.

**Table 8.** Summary of isolation factors, $if$, for the benchmark cases.

| Case | GF | HN | DP | TK | PH | RS | RR | BE |
|------|----|----|----|----|----|----|----|----|
| **HII40** | | | | | | | | |
| >1.01 | 8 | 5 | 1 | 17 | 2 | 4 | 7 | 8 |
| >1.03 | 5 | 3 | 0 | 15 | 1 | 3 | 5 | 6 |
| >1.10 | 3 | 0 | 0 | 8 | 0 | 2 | 1 | 5 |
| >1.30 | 0 | 0 | 0 | 5 | 0 | 0 | 0 | 3 |
| >2.00 | 0 | 0 | 0 | 2 | 0 | 0 | 0 | 0 |
| No pred. | 0 | 1 | 0 | 5 | 0 | 0 | 5 | 0 |
| **HII20** | | | | | | | | |
| >1.01 | 3 | 2 | 2 | 12 | 4 | 7 | 4 | 7 |
| >1.03 | 2 | 1 | 2 | 10 | 3 | 6 | 4 | 6 |
| >1.10 | 0 | 0 | 0 | 8 | 0 | 2 | 3 | 3 |
| >1.30 | 0 | 0 | 0 | 5 | 0 | 2 | 0 | 0 |
| >2.00 | 0 | 0 | 0 | 2 | 0 | 0 | 0 | 0 |
| No pred. | 0 | 2 | 0 | 1 | 0 | 0 | 3 | 0 |
| **PN150** | | | | | | | | |
| >1.01 | 4 | 8 | 2 | 27 | 15 | 23 | – | 6 |
| >1.03 | 4 | 6 | 2 | 26 | 13 | 19 | – | 5 |
| >1.10 | 1 | 2 | 0 | 22 | 7 | 16 | – | 1 |
| >1.30 | 0 | 0 | 0 | 17 | 6 | 7 | – | 0 |
| >2.00 | 0 | 0 | 0 | 7 | 2 | 2 | – | 0 |
| No pred. | 0 | 0 | 0 | 3 | 1 | 6 | – | 0 |
| **PN75** | | | | | | | | |
| >1.01 | 14 | 20 | 4 | – | 5 | 14 | – | 9 |
| >1.03 | 11 | 18 | 4 | – | 4 | 13 | – | 8 |
| >1.10 | 5 | 10 | 2 | – | 4 | 10 | – | 6 |
| >1.30 | 4 | 1 | 0 | – | 0 | 3 | – | 0 |
| >2.00 | 1 | 0 | 0 | – | 0 | 3 | – | 0 |
| No pred. | 1 | 1 | 0 | – | 1 | 4 | – | 0 |

**Table 9.** Summary of median values for the benchmark cases.

| Case | Total | GF | HN | DP | TK | PH | RS | RR | BE |
|------|-------|----|----|----|----|----|----|----|----|
| HII40 | 31 | 8 | 8 | 10 | 3 | 9 | 9 | 5 | 10 |
| HII20 | 24 | 4 | 7 | 7 | 3 | 11 | 6 | 4 | 5 |
| Subtot H II | | 12 | 15 | 17 | 6 | 20 | 15 | 9 | 15 |
| PN150 | 49 | 9 | 11 | 12 | 2 | 13 | 4 | – | 15 |
| PN75 | 40 | 10 | 8 | 19 | – | 16 | 13 | – | 13 |
| Subtot PN | | 19 | 19 | 31 | (2) | 29 | 17 | – | 28 |

# REFERENCES

Abbott D. C., Lucy L. B., 1985, ApJ, 288, 679
Aggarwal K. M., 1983, J. Phys. B, 16, 2405
Aggarwal K. M., 1984a, Sol. Phys., 94, 75
Aggarwal K. M., 1984b, ApJS, 56, 303
Aldrovandi S. M., Péquignot D., 1973, A&A, 25, 137
Allen C. W., 1973, Astrophysical Quantities. Athlone Press, Univ. London, London
Almog Y., Netzer H., 1989, MNRAS, 238, 57
Arnaud M., Raymond J., 1992, ApJ, 398, 394
Baesgen M., Diesch C., Grewing M., 1990, A&A, 201, 237
Balick B., Rugers M., Terzian Y., Chengalur J. N., 1993, ApJ, 411, 778
Balick B., Perinotto M., Maccioni A., Terzian Y., Hajian A. R., 1994, ApJ, 424, 800
Balick B., Hajian A. R., Terzian Y., Perinotto M., Patriarchi P., 1998, AJ, 116, 360
Balujia K. L., Zeippen C. J., 1988, J. Phys. B, 21, 1455
Bayes F. A., Saraph H. E., Seaton M. J., 1985, MNRAS, 215, 85
Benjamin R. A., Skillman E. D., Smits D. P., 1999, ApJ, 514, 307
Berrington K. A., 1988, J. Phys. B, 21, 1083

Berrington K. A., Burke P. G., Dufton P. L., Kingston A. E., 1981, Atomic Data Nucl. Data Tables, 26, 1
Bhatia A. K., Mason H. E., 1980, MNRAS, 190, 925
Bhatia A. K., Feldman U., Doscheck G. A., 1979, A&A, 80, 22
Bjorkman J. E., Wood K., 2001, ApJ, 554, 615
Boissé P., 1990, A&A, 228, 483
Brocklehurst M., 1972, MNRAS, 157, 211
Brown R. L., Matthews W. G., 1970, ApJ, 160, 939
Butler S. E., Zeippen C. J., 1994, A&AS, 108, 1
Castor J. I., 1974, ApJ, 189, 273
Corradi R. L. M., Perinotto M., Villaver E., Mampaso A., Gonçalves D. R., 1999, ApJ, 523, 721
Drake G. W. F., Ulrich H., 1980, ApJS, 42, 351
Drake G. W. F., Victor G. A., Dalgarno A., 1969, Phys. Rev., 180, 25
Dufton P. L., Kingston A. E., 1989, MNRAS, 241, 209
Dufton P. L., Kingston A. E., 1991, MNRAS, 248, 827
Dufton P. L., Keenan F. P., Hibbert A., Stafford R. P., Byrne P. B., Agnew D., 1991, MNRAS, 253, 474
Eidelsberg M., Crifo-Magnant F., Zeippen C. J., 1981, A&AS, 43, 455
Ercolano B., 2001, in Ferland G., Savin S. W., eds, ASP Conf. Ser. Vol. 247, Spectroscopic Challenges of Photoionized Plasmas. Astron. Soc. Pac., San Francisco, p. 281
Ercolano B., 2002, PhD thesis, Univ. London
Ercolano B., Morisset C., Barlow M. J., Storey P. J., Liu X.-W., 2003, MN-RAS, 340, 1153 (Paper II, this issue)
Fang Z., Kwong V. H. S., Parkinson W. H., 1993, ApJ, 413, 141
Ferland G. J., 1980, PASP, 92, 596
Ferland G. et al., 1995, in Williams R., Livio M., eds, STScI Symp. 8, The Analysis of Emission Lines. Cambridge Univ. Press, Cambridge, p. 83
Fischer O., Henning T., Yorke H. W., 1994, A&A, 284, 187
Flannery B. P., Roberge W., Rybicki G. B., 1980, ApJ, 236, 598
Fleming J., Brage T., Bell K. L., Vaeck N., Hibbert A., Godefroid M. R., Fischer C. F., 1995, ApJ, 455, 758
Fleming J., Bell K. L., Hibbert A., Vaeck N., Godefroid M. R., 1996, MN-RAS, 279, 1289
Flower D. R., 1968, ApJ, 2, L205
García-Segura G., 1997, ApJ, 489, 189
Gau J. N., Henry R. J. W., 1977, Phys. Rev. A, 16, 986
Giles K., 1981, MNRAS, 195, 63
Gruenwald R., Viegas S. M., de Broguiere D., 1997, ApJ, 480, 283
Harries T. J., Howarth I. D., 1997, A&AS, 121, 15
Harrington J. P., 1968, ApJ, 152, 943
Hayes M. A., Nussbaumer H., 1984, A&A, 134, 193
Hummer D. G., 1988, ApJ, 327, 477
Hummer D. G., 1994, MNRAS, 268, 109
Hummer D. G., Storey P. J., 1998, MNRAS, 297, 1073
Hummer D. G., Berrington K. A., Eissner W., Pradhan A. K., Saraph H. E., Tully J. A., 1993, A&A, 279, 298
Keenan F. P., Feibelman W. A., Berrington K. A., 1992, ApJ, 389, 443
Kingdon J. B., Ferland G. J., 1996, ApJS, 106, 205
Knigge C., Woods J., Drew J., 1995, MNRAS, 273, 225
Landini M., Monsignori Fossi B. C., 1990, A&AS, 82, 229
Landini M., Monsignori Fossi B. C., 1991, A&AS, 91, 183
Lefevre J., Bergeat J., Daniel J. V., 1982, A&A, 114, 341
Lefevre J., Daniel J. V., Bergeat J., 1983, A&A, 121, 51
Lennon D. J., Burke V. M., 1991, MNRAS, 251, 628
Lopez J. A., Meaburn J., Palmer J. W., 1993, ApJ, 415, L135
Lucy L. B., 1999, A&A, 344, 282
Lucy L. B., 2001, MNRAS, 326, L95
Lucy L. B., 2002, A&A, 384, L725
McLaughlin B. M., Bell K. L., 1998, J. Phys. B, 31, 4317
Mendoza C., 1983, in Flower D. R., ed., Proc. IAU Symp. 103, Planetary Nebulae. Reidel, Dordrecht, p. 143
Mendoza C., Zeippen C. J., 1983, MNRAS, 202, 981
Monteiro H., Morisset C., Gruenwald R., Viegas S. M., 2000, ApJ, 537, 853
Morisset C., Gruenwald R., Viegas S. M., 2000, ApJ, 533, 931
Nahar S. N., 2000, A&AS, 147, 549
Nahar S. N., Pradhan A. K., 1999, A&AS, 135, 347

Nussbaumer H., Rusca C., 1979, A&A, 72, 129

Nussbaumer H., Schmutz W., 1984, A&A, 138, 495

Nussbaumer H., Storey P., 1981, A&A, 96, 91

Nussbaumer H., Storey P. J., 1982, A&A, 115, 205

Nussbaumer H., Storey P. J., 1983, A&A, 126, 75

Nussbaumer H., Storey P. J., 1986, A&AS, 64, 545

Nussbaumer H., Storey P. J., 1987, A&AS, 69, 123

Och S. R., Lucy L. B., Rosa M. B., 1998, A&A, 336, 301

Osterbrock D. E., 1989, Astrophysics of Gaseous Nebulae and Active Galactic Nuclei. University Science Books, Mill Valley, CA

Osterbrock D. E., Wallace R. K., 1977, Astrophys. Lett., 19, 110

Pengelly R. M., 1964, MNRAS, 127, 145

Péquignot D., 1986, in Pequignot D., ed., Workshop on Model Nebulae. Observatoire de Meudon, Paris

Péquignot D., Aldrovandi S. M., 1976, A&A, 50, 141

Péquignot D., Stasinska G., Aldrovandi S. M. V., 1978, A&A, 63, 313

Péquignot D., Petitjean P., Boisson C., 1991, A&A, 251, 680

Péquignot D. et al., 2001, in Ferland G., Savin D. W., eds, ASP Conf. Ser. Vol. 247, Spectroscopic Challenges of Photoionized Plasmas. Astron. Soc. Pac., San Francisco, p. 533

Perinotto M., 2000, Ap&SS, 274, 205

Pradhan A. K., 1976, MNRAS, 177, 31

Ramsbottom C. A., Bell K. L., Keenan F. P., 1998, MNRAS, 293, 233

Reilman R. F., Manson S. T., 1979, ApJS, 40, 815

Robbins R. R., 1968, ApJ, 151, 497

Rubin R. H., 1968, ApJ, 153, 761

Sahai R., 2000, ApJ, 537, L43

Saraph H. E., Storey P. J., 1996, A&AS, 115, 151

Shull J. M., van Steenberg M., 1982, ApJS, 49, 351

Soker N., 1997, ApJS, 112, 487

Soker N., 2001, MNRAS, 324, 699

Stafford R. P., Bell K. L., Hibbert A., Wijesundera W. P., 1994, MNRAS, 268, 816

Storey P. J., 1981, MNRAS, 195, 27

Storey P. J., Hummer D. G., 1995, MNRAS, 272, 41

Thomas L. D., Nesbit R. K., 1975, Phys. Rev. A, 12, 2378

Verner D. A., Yakovlev D. G., 1995, A&AS, 109, 125

Verner D. A., Ferland G. J., Korista K. T., Yakovlev D. G., 1996, ApJ, 465, 487

Wiese W. L., Smith M. W., Glennon B. M., 1966, Atomic Transition Probabilities: Hydrogen through Neon, A Critical Data Compilation, NSRDS-NBS 4. US Department of Commerce, National Bureau of Standards, Washington, DC

Wolf S., Henning T., Secklum B., 1999, A&A, 349, 839

Zeippen C. J., 1982, MNRAS, 198, 111

Zhang H. L., Graziani M., Pradhan A. K., 1994, A&A, 283, 319

# APPENDIX A: ATOMIC DATA REFERENCES

Free–bound emission for hydrogenic ions (H I and He II): Ferland (1980)

Free–bound emission for He I: Brown & Matthews (1970)

Two-photon emission for hydrogenic ions (H I and He II): Nussbaumer & Schmutz (1984)

Two-photon emission for He I: Drake et al. (1969)

Free–free emission for interaction between ions of nucleus Z and electrons: Allen (1973)

Effective recombination coefficient to H I $2^2S$: Pengelly (1964)

Effective recombination coefficient to He I $2^1S$: Almog & Netzer (1989)

H I and He II recombination line emissivities: Storey & Hummer (1995)

He I recombination line emissivities: Benjamin et al. (1999)

Collision transition rates for H I $2^2S - 2^2P$: (page 94 Osterbrock 1989 page 94)

Cooling due to free–free radiation from hydrogenic ions (H I and He II): Hummer (1994)

Cooling due to free–free radiation from He I: Hummer & Storey (1998)

Cooling due to recombination of hydrogenic ions (H I and He II): Hummer (1994)

Cooling due to He I recombination: Hummer & Storey (1998)

Collisional ionization of hydrogen: Drake & Ulrich (1980)

Charge exchange with hydrogen: Kingdon & Ferland (1996)

Fits to calculate rates of radiative recombination for – H-, He-, Li- and Ne-like ions: Verner et al. (1996)

other ions of C, N, O and Ne: Péquignot, Petitjean & Boisson (1991)

Fe XVII–XXIII: Arnaud & Raymond (1992)

other ions of Mg, Si, S, Ar, Ca, Fe and Ni: Shull & van Steenberg (1982)

other ions of Na and Al: Landini & Monsignori Fossi (1990)

other ions of F, P, Cl, K, Ti, Cr, Mn and Co (excluding Ti I– II and Cr I–IV): Landini & Monsignori Fossi (1991)

Dielectronic recombination coefficients: Nussbaumer & Storey (1983); Nussbaumer & Storey (1986); Nussbaumer & Storey (1987)

Non relativistic free–free Gaunt factor for hydrogenic ions: Hummer (1988)

Fits to Opacity Project data for the photoionization cross-sections (outer shell): Verner et al. (1996)

Collision strengths and transition probabilities to calculate collisionally excited line strengths from ions:

C I Collision strengths from Péquignot & Aldrovandi (1976); $^5S$–$^3P$ from Thomas & Nesbit (1975). Transition probabilities from Nussbaumer & Rusca (1979).

C II Collision strengths from Hayes & Nussbaumer (1984). Transition probabilities from Nussbaumer & Storey (1981).

C III Collision strengths and transition probabilities from Keenan, Feibelman & Berrington (1992) and Fleming et al. (1996).

C IV Collision strengths from Gau & Henry (1977). Transition probabilities from Wiese, Smith & Glennon (1966).

Mg I Collision strengths from Saraph & Storey (1996) JAJOM calculations. Transition probabilities from Mendoza (1983).

Mg II Collision strengths and transition probabilities from Mendoza (1983).

Mg IV Collision strengths from Butler & Zeippen (1994). Transition probabilities from Mendoza & Zeippen (1983).

Mg V Collision strengths from Butler & Zeippen (1994). Transition probabilities from Mendoza (1983).

Mg VI Collision strengths from Bhatia & Mason (1980). Transition probabilities from Eidelsberg et al. (1981).

Mg VII Collision strengths from Aggarwal (1984a) and Aggarwal (1984b). Transition probabilities from Nussbaumer & Rusca (1979).

Ne II Collision strengths from Bayes et al. (1985). Transition probabilities from Mendoza & Zeippen (1983).

Mg III Collision strengths from Butler & Zeippen (1994). Transition probabilities from Mendoza & Zeippen (1983).

Ne IV Collision strengths from Giles (1981). Transition probabilities from Zeippen (1982).

Ne V Collision strengths from Lennon & Burke (1991). Transition probabilities from Nussbaumer & Rusca (1979).

Ne VI Collision strengths from Butler & Storey (unpublished). Transition probabilities from Wiese et al. (1966).

N I Collision strengths from Berrington et al. (1981). Transition probabilities from Zeippen (1982).

N II Collision strengths from Stafford et al. (1994). Transition probabilities from Nussbaumer & Rusca (1979).

N III Collision strengths from Nussbaumer & Rusca (1979), rescaled to Nussbaumer & Storey (1982); fine-structure terms from Butler & Storey (unpublished). Transition probabilities from Fang et al. (1993).

N VI Collision strengths from Mendoza & Zeippen (1983). Transition probabilities from Nussbaumer & Rusca (1979) and Fleming et al. (1995).

N V Collision strengths from Osterbrock & Wallace (1977). Transition probabilities from Wiese et al. (1966).

O I Collision strengths from Berrington et al. (1981) and Berrington (1988). Transition probabilities from Balujia & Zeippen (1988).

O II Collision strengths from Pradhan (1976). Transition probabilities from Zeippen (1982).

O III Collision strengths from Aggarwal (1983). Transition probabilities from Nussbaumer & Storey (1981).

O IV Collision strengths from Zhang, Graziani & Pradhan (1994) and from Hayes & Nussbaumer (1984). Transition probabilities from Nussbaumer & Storey (1982).

O V Collision strengths and transition probabilities from Mendoza (1983).

O VI Collision strengths and transition probabilities from Mendoza (1983).

Si II Collision strengths from Dufton & Kingston (1991). Transition probabilities from Mendoza & Zeippen (1983) and from Dufton et al. (1991).

Si III Collision strengths from Dufton & Kingston (1989). Transition probabilities from Mendoza & Zeippen (1983)

Si IV Collision strengths and transition probabilities from Mendoza (1983).

Si VII Fine-structure collision strengths from Butler (unpublished). Transition probabilities from Bhatia et al. (1979).

S II Collision strengths from Mendoza & Zeippen (1983). Transition probabilities from Mendoza (1983).

S III Collision strengths from Mendoza & Zeippen (1983). Transition probabilities from Mendoza (1983)

S IV Collision strengths from Saraph & Storey (1996). Transition probabilities from Storey (unpublished)

This paper has been typeset from a TEX/LATEX file prepared by the author.